UNIVERSITY OF CALIFORNIA, SAN DIEGO

Control of structure and properties of functional materials

A dissertation submitted in partial satisfaction of the requirements for the degree

Doctor of Philosophy

in

Materials Science and Engineering

by

Chin-Hung Liu

Committee in charge:

Professor Sungho Jin, Chair
Professor Renkun Chen, Co-Chair
Professor Olivia Graeve
Professor Ratneshwar Lal
Professor Yu Qiao

2016

THE DISSERTATION OF CHIN-HUNG LIU IS APPROVED, AND IT IS ACCEPTABLE IN QUALITY AND FORM FOR PUBLICATION ON MICROFILM AND ELECTRONICALLY:

Co-Chair

Chair

University of California, San Diego

2016

DEDICATION

To my grandfather, Zai-Sheng Liu, who taught me the quintessence of virtue.

EPIGRAPH

Blessed is every one that feareth the LORD; that walketh in His ways.

For thou shalt eat the labour of thine hands: happy shalt thou be, and it shall be well with thee.

Thy wife shall be as a fruitful vine by the sides of thine house: thy children like olive plants round about thy table.

Behold, that thus shall the man be blessed that feareth the LORD.

Psalm 128:1-4

TABLE OF CONTENTS

LIST OF ABBREVIATIONS

SEM: Scanning Electron Microscopy

EDS: Energy Dispersive Spectrum

XRD: X-Ray Diffraction

TEM: Transmission Electron Microscopy

HRTEM: High-Resolution Transmission Electron Microscopy

DSC: Differential Scanning Calorimetric

SB: Sn-Bi

SBM2: Sn-Bi-2wt%mischmetal

SBM4: Sn-Bi-4wt%mischmetal

SBIM4: Sn-Bi-10wt%In-2wt%mischmetal

AlN: Aluminum Nitride

BK7: Boroscilicate glass Schott

KTP: Potassium Titanyl Phosphate

LBO: Lithium Triborate

LTP: Low Temperature Phase

HH: Half-Heusler

SE: Spark Erosion

HH550: Half-Heusler SE particles sintered at 550 °C

HH1100: Half-Heusler SE particles sintered at 1,100 °C

LIST OF SYMBOLS

K_{α}: Characteristic wavelength of electrons emitted from 2p orbital to K shell.

ZT: Figure of merit.

H_c: Coercivity

M_s: Magnetization

$(BH)_{max}$: Energy product

$2b_m$: Width of soft m-magnet's domain wall

$2b_k$: Width of hard k-magnet's domain wall

σ: Electrical conductivity

θ: degree

kg: Kilogram

LIST OF FIGURES

LIST OF TABLES

ACKNOWLEDGEMENTS

I would like to acknowledge Professor Sungho Jin for his support and guidance through all my time at UCSD.

I would like also to acknowledge Professor Renkun Chen for his suggestions and guidance about my experimental design and process especially on hot press related process.

I would like also to acknowledge Dr. Li-Han Chen for his advices and guidance. His teaching on magnetism has proved to be invaluable.

Chapter 1, in full, is a reprint of the material as it appears in Materials Letters, vol. 152, pp. 232-236, 2015. The dissertation author was the primary investigator and author of this paper. Co-authors include, Young Jin Kim, Dong Won Chun, Gunwoo Kim, Renkun Chen, Anthony W. Yu, and Sungho Jin.

Chapter 2, in part, is currently being prepared for submission for publication of the material. The dissertation author was the primary investigator and author of this paper. Co-author include Sungho Jin.

Chapter 3, in full, is currently being prepared for submission for publication of the material. The dissertation author was the primary investigator and author of this paper. Co-authors include DongWon Chun, Renkun Chen and Sungho Jin.

I’ve learned how to dream, I’ve been taught how to be practical, I’ve been trained how to fulfill my ideas and dreams. I had been staying in universities for more than a decade and it is time for me to see the world, to experience things dangerous to come to, to see behind the academic walls, to draw closer to my inner self, to find it and to feel it. That’s the plan for my future.

VITA

2007 Bachelor of Science, National Cheng Kung University, Tainan, Taiwan

2011 Master, National Tsing Hua University, Hsinchu, Taiwan

2011-2016 Research Assistant, University of California, San Diego, USA

2016 Doctor of Philosophy, University of California, San Diego, USA

PUBLICATIONS

1. *Chin-Hung Liu*, Young Jin Kim, Dong Won Chun, Gunwoo Kim, Renkun Chen, Anthony W. Yu, Sungho Jin, "Universal solders for direct bonding and packaging of optical devices", *Materials Letters*, 152, 232-236, 2015.
2. Yu-Lun Chueh, *Chin-Hung Liu*, and Chih-Huang Lai, *Method for Making a Solar Cell*, US Patent USPTO No. US 20130029451 A1, 2013.
3. *Chin-Hung Liu*, Szu-Ying Chen, Cheng-Ying Chen, Jr-Hau He, Lih-Juann Chen, Johnny C. Ho, and Yu-Lun Chueh, "Kinetic Growth of Self-Formed In2O3 Nanodots via Phase Segregation: Ni/InAs System," *ACS Nano,* vol. 5, no. 8, pp. 6637-6642, 2011.
4. *Chin-Hung Liu*, Chia-Hsiang Chen, Szu-Ying Chen, Yu-Ting Yen, Wei-Chen Kuo, Yu-Kuang Liao, Jenh-Yih Juang, Hao-Chung Kuo, Chih-Huang Lai, Lih-Juann Chen, and Yu-Lun Chueh, "Large Scale Single-Crystal Cu(In,Ga)Se2 Nanotip Arrays For High Efficiency Solar Cell," *Nano Letters,* vol. 11, no. 10, pp. 4443-4448, 2011.

FIELDS OF STUDY

Packaging materials, permanent magnets, thermoelectrics, solar cells, LEDs.

Major Field: MSE

ABSTRACT OF THE DISSERTATION

Control of structure and properties of functional materials

by

Chin-Hung Liu

Doctor of Philosophy in Materials Science and Engineering

University of California, San Diego, 2016

Professor Sungho Jin, Chair

Professor Renkun Chen, Co-Chair

Functional materials mean materials that have broad application yet specific function that cannot be easily substituted with other materials. In this dissertation, we mainly focus on functional materials, such as solder, permanent magnets and thermoelectric materials. Here we discussed how to control functional materials' structure and properties and improvement of their performance. We also provided practical examples and in depth study in MSE.

INTRODUCTION

This dissertation is mainly focused on the study of functional materials. Functional materials include solders for semiconductor and chip device industry, permanent magnets for hybrid vehicles and wind turbine industry, and thermoelectric material for renewable energy industry. Therefore, all above-mentioned functional materials have great commercial potential and deserve extensive and systematic study.

Solder is mainly used for electronic devices packaging process, which is to connect functional chips with frames so that the chip became portable and compatible with various devices. However, because regular solder can make bonding only on metals, scientists and engineers have to make extra efforts to overcome this limitation, and this requirement of extra metallization and associated processes make the packaging process more complicated and costly. Therefore, solders that can bond directly onto silicon, oxide, and various functional ceramic at regular working temperatures are highly desired. Here we combine metallurgy and knowledge of thermodynamics to fabricate “Universal Solder” that can make direct and strong bonding on metal and almost all inorganic materials.

Permanent magnets with high energy product, $(BH)_{max}$, are extensively used in various motors and generators, including electric motors in hybrid vehicles and wind turbines. The higher the $(BH)_{max}$, the lighter the permanent magnet can be for the same motor efficiency. In terms of electromagnet application, higher $(BH)_{max}$ also means higher energy efficiency.

Scientists and engineers around the world are trying to enhance the current standard of $(BH)_{max}$ and the working temperature. Here we proposed a novel coating technique for making high $(BH)_{max}$ permanent magnet.

Waste heat was produced everyday and everywhere not only in the United States but around the world. Wasted heat can be produced from personal computers, household appliances, vehicles, industry activities and power plant. In order to effectively transform such wasted heat energy into renewable energy, high quality thermoelectric materials are necessary. Here we proposed a novel process to fabricate a thermoelectric material based on half-Heusler alloy.

CHAPTER 1: UNIVERSAL SOLDERS FOR DIRECT BONDING AND PACKAGING OF OPTICAL DEVICES

INTRODUCTION

Modern laser and telecommunications technologies involve extensive use of a variety of optical materials and crystals, which often requires a direct assembly and packaging of optical oxide components and structures. Some of the optical crystal materials are quite sensitive to exposure to high temperatures, and hence a low temperature bonding of such optical crystals is highly desirable. There are many solders and related bonding materials utilized for assembly of electronic and optical devices [1-3]. However, commercially available common solders, such as Sn-Pb, Sn–Ag, Sn-Au, Sn-Bi, and Sn-Cu, cannot directly make reliable bonding on oxide, nitride, sulfide, silicon and other non-metallic substrates [3]. One of the well known techniques to make these solders to bond onto these non-metallic substrate is to deposit a thin metallization layer that is solderable onto these substrate surface before soldering. Such metallization techniques include evaporation deposition [4], sputter deposition [4] and electrodepostion [5]. However, the deposited metal layer does not always have strong bonding onto the substrate surface, and the usable substrate dimension/geometry is limited by the deposition chamber or deposition technique, especially if the substrate in not in a planar geometry.

It was reported that rare-earth metal dopants can significantly enhance solder bonding with these non-metallic substrates [6-9] because rare-earth metals have a stronger affinity for oxygen, nitrogen or carbon, and hence

reduces oxides, nitrides and carbides to form strong chemical bonding at the interface [8,10]. Previous research on rare-earth-containing solder has mostly focused on elemental rare-earth [11, 12], which are quite expensive. Here we chose relatively inexpensive mischmetal as the rare-earth containing dopant to create solders that can directly bond onto oxides and nitrides, especially in a lower temperature solder of Bi-Sn to allow optical crystal bonding in a safe manner. With this mischmetal containing solders, it is demonstrated that optical oxide materials can easily and directly be bonded onto substrate without using interfacial thin film deposition.

Solder Fabrication Process

Sn-42wt% Bi eutectic alloy (99.95% purity), mischmetal (99.0% purity) and indium (99.99% purity) were purchased from Alfa Aesar. We prepared three different types of solder alloys by doping Sn-Bi alloy (SB) with 2 wt % mischmetal (SBM2), 4 wt % mischmetal (SBM4) and a combination of 10 wt % indium plus 4 wt % mischmetal (SBIM4) to explore further lowered solder alloy melting points. The mischmetal is mainly composed of cerium (~ 50 wt%) and lanthanum (~25 wt%) with small amounts of impurity rare earth such as neodymium and praseodymium. As the mischmetal is an unpurified alloy, it is much cheaper than common elemental rare-earth metals previously utilized for making universal solders that can bonds onto oxide and nitride surfaces [6, 8]. The mischmetal-doped Sn-Bi solder was fabricated as follows. As shown in Figure 1-1(a), both Sn-Bi solder and mischmetal were placed inside a quartz tube. The mischmetal was attached on a nickel wire that was fixed onto a ferromagnetic rod. A

magnetic maneuver setup based on a strong Nd-Fe-B magnet was positioned outside the quartz tube to hold and maneuver the vertical position of this ferromagnetic rod and attached mischmetal piece. The Sn-Bi solder was melted first inside the quartz tube under ~1 x 10^{-4} Torr vacuum, and then the mischmetal was lowered into the molten solder by pulling down the Nd-Fe-B magnet from outside of the quartz tube. This magnetically guided up-and-down disturbing movement was repeated several times to make sure full dissolution of mischmetal in the Sn-Bi molten solder and to enhance compositional homogenization of the final alloy ingot. The molten alloy was then air quenched by blasting the outside surface of the quartz tube with compressed air flow. The solidified mischmetal-doped Sn-Bi solder was then retrieved from the quartz tube and used for bonding of optical crystal materials on various substrates including aluminum nitride (AlN), Schott borosilicate glass (BK7), potassium titanyl phosphate (KTP), and lithium triborate (LBO).

Before solder bonding, all substrates were preheated to 100^{o}C by placing on a hot plate in air with, continuous monitoring of temperature with a thermocouple. A hand-soldering process was performed by picking a small piece of solder with the soldering gun tip then smearing the molten solder onto the desired substrate surface within a few seconds. As shown in Figure 1-1 (b), shear strength of the bonded junction was evaluated by mechanical pulling or weight-activated pulling of a nickel or copper wire that was solder bonded on the optical crystal substrate. The solder microstructures and compositions were evaluated with Scanning Electron Microscopy (SEM, FEI XL30) equipped with an

energy dispersive X-ray Spectroscopy (EDS) analysis system. Crystal structures of fabricated solder alloys were characterized by Bruker D2 Phaser X-ray diffractometer (XRD) with Cu K_α (λ=0.154 nm) as the radiation source and θ-2θ scan range was set from 20^o to 80^o. The solder melting points were determined by differential scanning caloimetry (DSC, Perkin Elmer DSC8000).

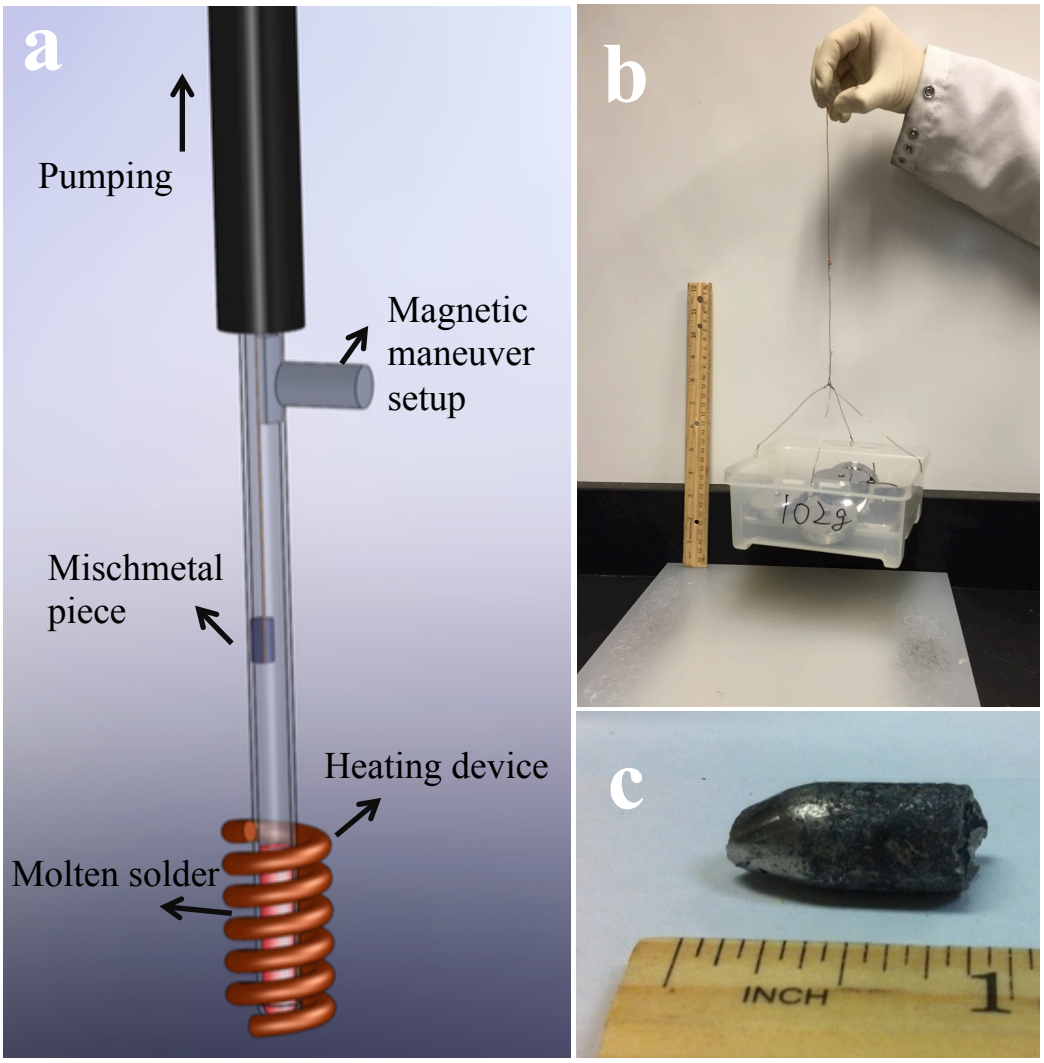

Figure 1-1 Fabrication scheme of mischmetal containing Sn-Bi solders and the testing of bond shear strength. (a) Schematic illustration of mischmetal-doped universal solder fabrication process. (b) SBM4 solder bonded on BK7 crystal substrate pulled by total 1.7 kg weights, which equals to 80 psi shear stress. (c) Sn-Bi-10wt%-4wt%mischmetal universal solder alloy.

Results and Discussion

The lead-free, mischmetal-doped Sn-Bi solder alloy we made was presented in Figure 1-1 (c). The size was 1 inch long with diameter of ½ inch and this size can be easily scale up and even incorporate into massive production process.

In order to test bond shear strengths of the lead-free Sn-Bi-mischmetal solders on nitrides and oxide crystal materials, we directly bonded nickel or copper wires (500 μm diameter) onto the substrates without using any pre-metallization coating. Figure 1-1 (b) shown how the bond shear strength was tested. The bonded copper wire was pulled in a direction parallel to the substrate surface and the bond shear strength was calculated by dividing the loading weight with bonded junction interfacial area. Figure 1-1 (b) shows the bonded assembly of SBM4 solder on non-linear optical crystal BK7, with the bonded junction pulled down with weights inside a basket. The total weight is 1,700 grams, which is equivalent to 80 pounds per square inch (psi) bond shear strength in this case. As indicated in Table 1-1, Sn-Bi based solder doped with mischmetal produced reliable bonding to various substrates. Many of the optical crystals are anisotropic with layered structure and hence the solder bond too these crystals tend to be not as strong as regular oxides or nitrides. The bond shear strength of Sn-Bi-mischmetal is greater than 150 psi on aluminum nitride, greater than 22 psi on KTP and greater than 30 psi on LBO.

Figures 1-2 (a) and 1-2 (b) shown the crystal structure and melting point of universal solders fabricated by process illustrated in Figure 1-1 (a). As indicated in Figure 1-2 (a), we can observe tin peak (denoted as black square) and bismuth peak (denoted as red circle) form x-ray diffraction patterns of as-received SB, SBM2 and SBM4 solders. The basic crystal structure of Sn-Bi matrix solder was not affected by mischmetal dopant. As indicated in Figure 1-2 (b), mischmetal dopant didn't affect the onset melting point of the SB matrix solder we used for this research and SB, SBM2 SBM4 solders all have melting point close to the melting point of Sn-Bi eutectic alloy (~139^{o}C). Based on these two factors, we concluded that we have a uniform Sn-Bi eutectic solder alloy matrix and both SBM2 and SBM4 solders have identical melting point as regular SB solder but with good bonding ability on nitrides and oxides. Figure 1-2 (a) also shows x-ray diffraction pattern of SBIM4 solder. Besides Sn and Bi, Ce_3In and BiIn intermetallic compounds (IMC) were formed by doping the Sn-Bi solder matrix with indium and mischmetal in the solidified state, however, it is possible that in the molten state, these intermetallic islands can dissolve into the molten solder and make the rare earth atoms available for strong interfacial reaction and bonding.

For some optical bonding applications, even further lowered melting point together with strong bondability is highly desirable. To this end, we have investigated an additional modification of the solder composition by also doping with indium (In), in addition to the mischmetal. A combination of 10 wt % indium plus 4 wt % mischmetal (SBIM4) was used for doping of Sn-Bi eutectic matrix

solder. The melting points of BiIn and related intermetallic phases are lower than 100^{o}C so the SBIM4 solder alloy with indium and mischmetal combination dopant can have a further suppressed melting point of ~104^{o}C as compared to the ~140^{o}C melting point of SBM4 alloy containing only mischmetal dopant as shown in Table 1-1. The low melting point we observed (104^{o}C) provides one of the lowest working temperatures of universal solders ever reported. The ability to make strong bonding with nitride, oxide and other non-metallic substrate at such a low temperature of ~100^{o}C can create new possibilities for producing advanced MEMS, flexible plastic substrate based System-on-Chips, and even re-invent some of assembly schemes in the packaging industry [13]. Melting points and bond shear strength of each universal solder were summarized in Table 1-1.

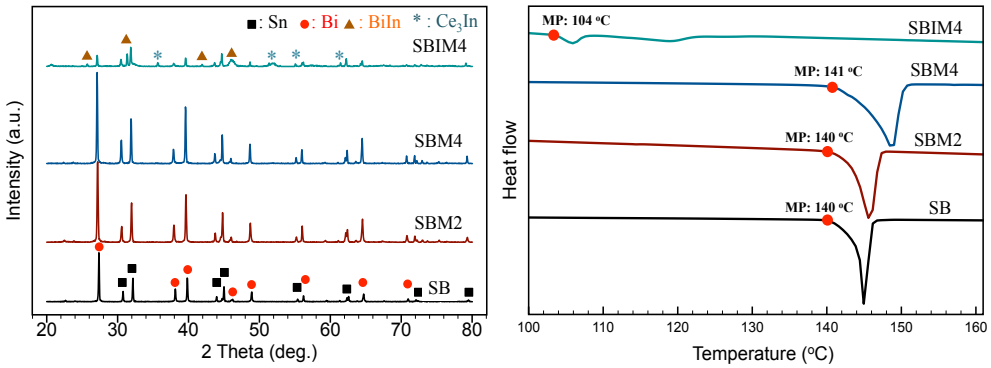

Figure 1-2 Crystal structure and melting point of SB, SBM2, SBM4 and SBIM4 solder alloys. (a) X-ray diffraction patterns. Signals from Sn, Bi, BiIn and Ce_3In phases are identified. (b) DSC profile of SB, SBM2, SBM4 and SBIM4 universal solders.

Table 1-1 Summary of solder melting point and bond shear strength on substrates.

Substrate	Solder	Solder melting temperature (^{o}C)	Bond shear strength (psi)
Aluminum Nitride (AlN)	SBM4	140	> 150
Schott Borosilicate glass (BK7)	SBM4	140	> 80
Potassium Titanyl Phosphate (KTP)	SBM4	140	> 22
Lithium Triborate (LBO)	SBIM4	104	> 30

The doping of Sn-Bi solder with mischmetal (and also indium) affects microstructural features. Shown in Figures 1-3 (a) - (d) are the effect of mischmetal doping on Sn-Bi solder matrix microstructure. The globular structure of Sn-Bi eutectic solder alloy is shown in Figure 1-3 (a), with corresponding element mapping of Sn-rich phase (red) and Bi-rich (green) phase shown in Figure 1-3 (c). The microstructure and element mapping of Sn-Bi eutectic solder alloy doped with 2 wt% mischmetal are shown in Figure 1-3 (b) and 1-3 (d), respectively. As indicated in Figure 1-3 (d), Sn-rich (red) and Bi-rich (blue) phases are uniformly distributed while cerium (green), one of the major components of mischmetal, tends to segregate into micro size grains because cerium and lanthanum in mischmetal both have limited solubility in Sn and Bi [14].

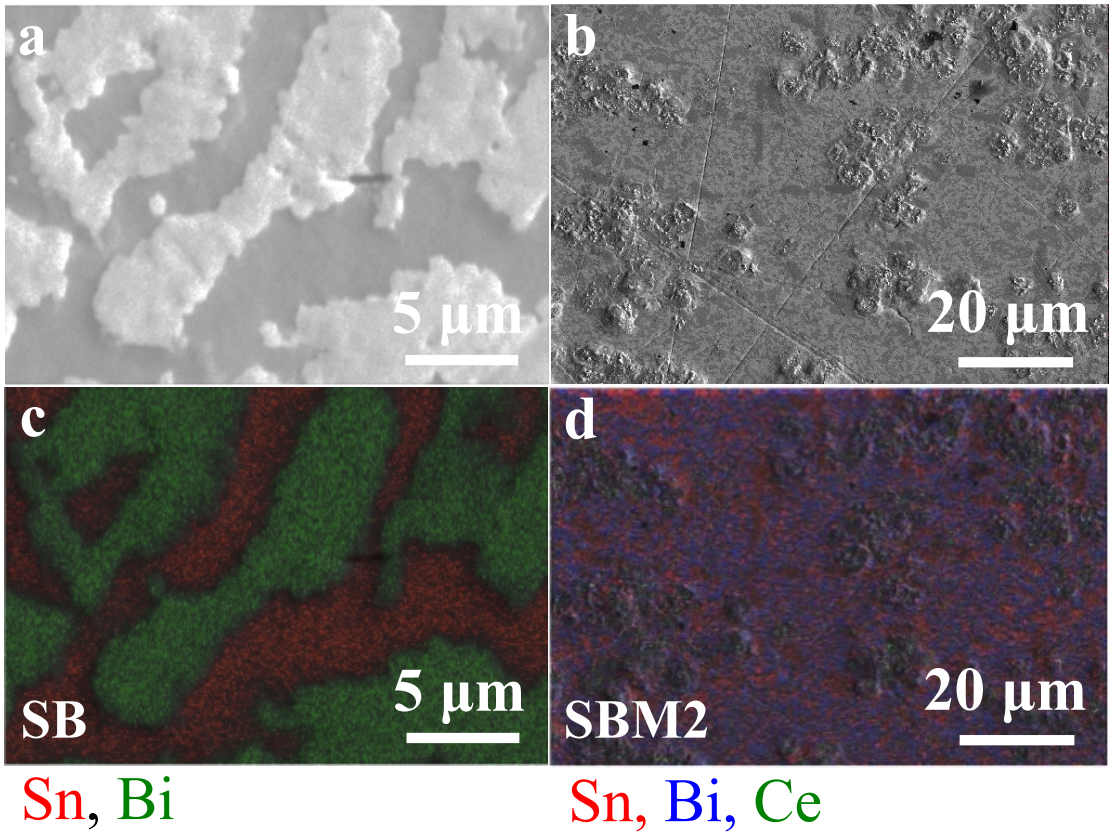

Figure 1-3 Microstructure and elemental mapping solder alloys. (a) Microstructure of SB solder alloy. (b) Microstructure of SBM2 solder alloy. (c) Elemental mapping of SB solder alloy with Sn-rich (red) and Bi-rich (green) regions as indicated. (d) Elemental mapping of mischmetal doped SB solder alloy with Sn-rich (red), Bi-rich (blue) and Ce-rich (green) regions as indicated.

Figures 1-4 (a)-(d) show the effect of doping 10 wt% indium on the microstructure of Sn-Bi-4wt% mischmetal solder alloy. As shown in Figures 1-4 (a) and 1-4 (c), Sn-rich (red) and Bi-rich (purple) regions are uniformly distributed and both Ce (blue) and La (green) rare-earth metal tend to segregate into large grains. By comparing Figures 1-3 (b) and 1-4 (a), we can observe that as the concentration of doped mischmetal increased from 2 wt% to 4 wt%, the density of mischmetal-containing grain increased and elemental mapping signals from both cerium and lanthanum rare-earth metals were observed as they are the main components of mischmetal. The microstructure and elemental mapping of SBIM4 solder are shown in Figures 1-4 (b) and 1-4 (d), respectively. Sn (green), Bi (yellow) and In (red) are uniformly mixed and both Ce (purple) and La (blue) segregated into large grains and randomly distributed in the Sn-Bi-In solder matrix. According to XRD and DSC results shown in Figure 1-2 (a) and 1-2 (b), Ce_3In and BiIn IMC were formed and the melting point of SBIM4 was suppressed down to 104^{o}C. Such a low melting temperature solder is useful for minimizing and even preventing thermal shock between solder and the substrate materials during soldering process [1]. Uniformly distributed indium and michmetal rich islands can also contribute to grain refinement and help to reduce creep and fatigue crack formation [9], however, further research is required to confirm such a behavior in SBIM4 universal solder alloy.

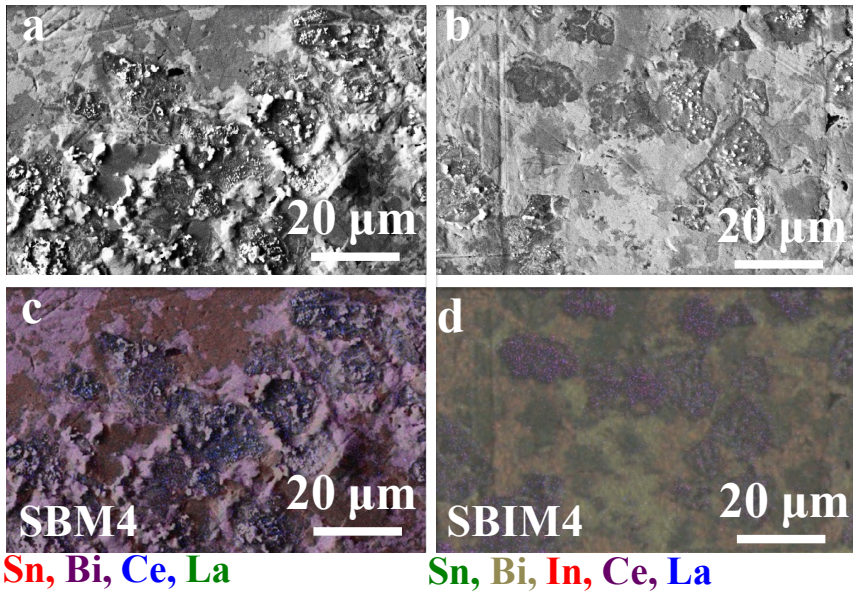

Figure 1-4 Microstructure and elemental mapping of solder alloys. (a) Microstructure of SBM4 solder alloy. (b) Microstructure of SBIM4 solder alloy. (c) Elemental mapping of SBM4 solder alloy with Sn-rich (red), Bi-rich (purple), Ce-rich (blue) and La-rich (green) regions as indicated. (d) Elemental mapping of SBIM4 solder alloy with Sn-rich (green), Bi-rich (yellow), In-rich (red), Ce-rich (purple) and La-rich (blue) regions as indicated.

Shown in Figures 1-5 (a) – (d) are microstructures of the SBM4 and SBIM4 solders bonded on Schott borosilicate glass (BK7), potassium titanyl phosphate (KTP), lithium triborate (LBO) and aluminum nitride (AlN) substrates, respectively. Figure 1-5 (e) shown the elemental mapping of SBM4 solder bonded on AlN substrate. Both Sn-rich (green) and Bi-rich (purple) regions are uniformly distributed in the solder matrix and Ce-rich (blue) region is segregated near the interface. It was found that the SBM4 solder formed a continuous smooth interface with underlying AlN (red) substrates. The bond shear strength is strong and in excess of 150 psi for SBM4 on AlN substrate.

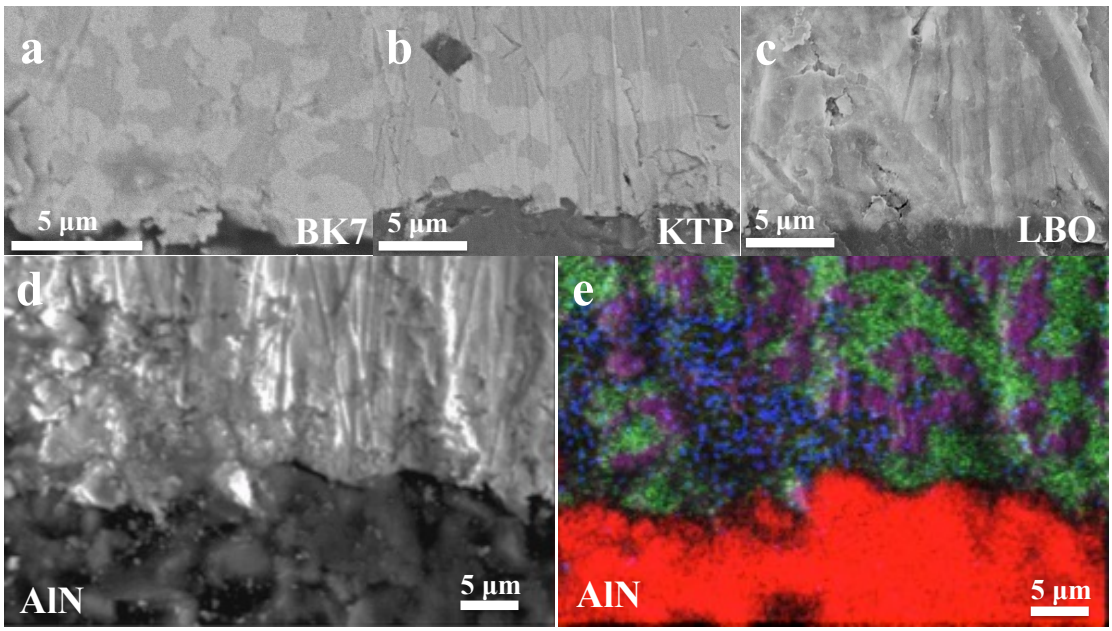

Figure 1-5 Microstructure and element mapping of solder to substrate interfaces. (a) Microstructure of SBM4-BK7 interface. (b) Microstructure of SBM4-KTP interface. (c) Microstructure of SBIM4-LBO interface. (d) Microstructure of SBM4-AlN interface. (e) Element mapping of SBM4 solder alloy and AlN substrate with Sn-rich (green), Bi-rich (purple), Ce-rich (blue) and AlN-rich (red) regions as indicated.

As shown in Figures 1-4 (a) – (d), mischmetal-rich grains are surrounded by Sn-Bi solder matrix, which serves the purpose of preserving the reactive mischmetal as embedded/protected islands within the alloy before use for bonding. During soldering, fresh mischmetal-containing grains will participate in the solder melting process, with the reactive metallic components in the mischmetal becoming active which will form strong chemical bonding with substrate surface within seconds. Rare-earth metals tend to easily form compounds with nitride and oxide. It is because the heat of formation of rare-earth nitride or rare-earth oxide such as with cerium or lanthanum is more negative (more stable) than those nitrides or oxides such as AlN, BK7, LBO, and KTP substrates. Therefore, these rare-earth containing compounds are thermodynamically favorable and chemically more stable [15], thus providing a stable and strong interfacial bonding. After solder bonding is completed with universal solders and the solder joint begins to solidify, the remaining mischmetal grains will be surrounded again by Sn-Bi matrix. Therefore with the rare-earth elements are buried and protected, until next melting events occur. By comparing Figures 1-3 (b) and 1-4 (a), because SBM4 solder had more rare-earth metals relatively uniformly distributed inside it, SBM4 has higher bond shear strength than solder contains only 2 wt% mischmetal. One aspect to note is that the interfacial bond strengths with these optical crystals such as BK7, LBO, and KTP substrates, while adequate, are in general lower than the bond strengths for the higher m.p. universal solders based on Sn-Ag or Au-Sn eutectic systems on isotropic oxides such as SiO_2 or Al_2O_3. This is partly is attributed to the

anisotropic or layered structure of these optical crystals, which allows an easier fracture in general. Another factor might be due to the much lower bond temperatures used (150^{o}C regime in this Sn-Bi eutectic based universal solders) than those for the Sn-Ag or Au-Sn universal solders (250 – 320^{o}C regime). Further research is required to thoroughly study the effects of crystal layer structure and soldering temperature on bond strength. The good bond shear strength from the universal solder bonding is tentatively attributed to the strong chemical-reaction bonding involving rare-earth elements at the solder-substrate interface. In order to fully understand the mechanism, further extensive TEM analyses are required.

Summary of Universal Solder Section

In summary, we have demonstrated that by doping a small amount (2 - 4 wt%) of mischmetal into lead-free Sn-Bi eutectic solder alloy, we can make solders to make a direct and strong bonding to nitride and oxide substrates including non-linear optical crystals, at a low temperature regime of ~150^{o}C or lower. The use of much more inexpensive mischmetal as the dopants instead of costly rare earth elemental metals will be beneficial for industrial application of the universal solders. The bond shear strength was tested by directly pulling a metal wire that was bonded on the substrate with the mischcmetal-doped, low melting point, Sn-Bi eutectic universal solder. Ce and La, the two main components of mischmetal, were detected by EDS elemental mapping to be distributed inside universal solder and on the interface between the solder and

the underlying substrate. Additional indium doping can further reduce universal solder melting temperature to 104^{o}C so that such a universal solder can advantageously be applied to thermal-shock-sensitive substrates.

ACKNOWLEDGEMENTS

The authors acknowledge the financial support of this work by Iwama Endowed Fund at UC San Diego and NASA Goddard Space Flight Center.

Chapter 1, in full, is a reprint of the material as it appears in Materials Letters, vol. 152, pp. 232-236, 2015. The dissertation author was the primary investigator and author of this paper. Co-authors include, Young Jin Kim, Dong Won Chun, Gunwoo Kim, Renkun Chen, Anthony W. Yu, and Sungho Jin.

CHAPTER 2: NEW GENERATION HYBRID MAGNETS COMPOSED OF HARD/SOFT MAGNETS

INTRODUCTION

Magnets are used in various applications, such as loudspeakers, household appliances, generators for wind turbines and electric motors for hybrid vehicles [16,17]. For wind turbines and hybrid vehicles, one of the most important properties is their energy product $(BH)_{max}$. Energy product is based on both magnetization (M_s) and coercivity (H_c) according to magnetism. We can enhance magnets' energy product by increasing its magnetization and coercivity or increase both factors at the same time.

We may be able to enhance magnets' coercivity by restrain magnetic domains from moving and/or rotating. We can also increase its magnetization by controlling magnets components, crystal structure and purity [18-20].
Another method is to make exchange coupling magnets [21].

Exchange coupling is an interaction between magnetization direction, the easy axes, in soft-magnet (m-magnet) and hard-magnet (k-magnet) and its mechanism is described in Figure 2-1. In this figure, $2b_m$ is the width of soft magnet and $2b_k$ is the width of hard magnet. The arrangement of easy axes in both m-magnets and k-magnets are depicted in Figure 2-1 (a). with an increasing external magnetic field, H, the easy axes in m-magnet will begin to change while easy axes in k-magnet stay unchanged because of higher magnetocrystalline anisotropy in k-magnet than in m-magnet. Figure 2-1 (b) shown the easy axes

arrangement in this initial stage. As the external magnetic field further increased, as shown in figure 2-1 (c), the reversed easyaxes will move toward k-magnet, and energy density in m-magnet will exceed its equilibrium value, therefore, the width of m-magnet decreased and reversed easy axes were pushed further toward k-magnet. As shown in figure 2-1 (d), once energy density in m-magnet approaches the energy density in k-magnet, the width of m-magnet is further decreased and the easy axes in k-magnet start flip. It has been shown that magnetic nanocomposite's energy product can be enhanced by making exchange coupled structure [22]. Here we proposed two different processes on making exchange coupled bulk magnets and discuss how magnets' properties are related to process conditions.

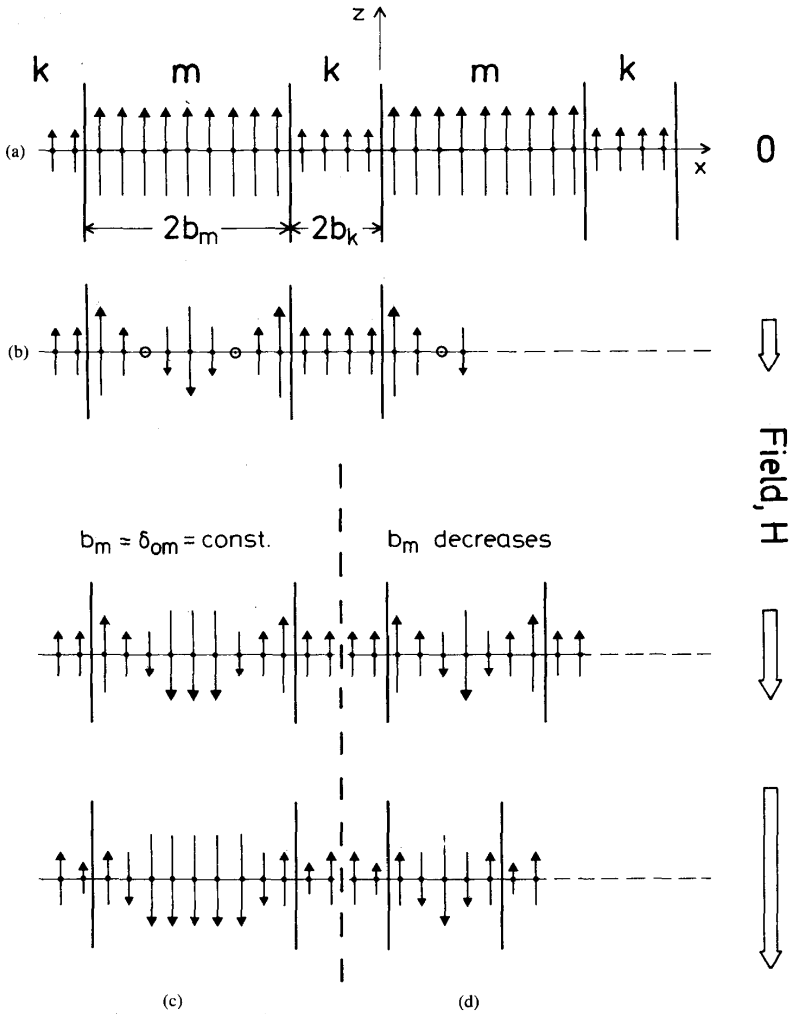

Figure 2-1 Exchange coupling mechanism. Soft-magnet (m-magnet) and hard-magnet (k-magnet) and their width $2b_m$, $2b_k$ are as described. and its is described. (a). No external field, (b). Under slight external magnetic field, (c). Under mild external magnetic field, (d). Under strong external magnetic field.

The strongest commercially available magnet is Dy-doped Nd-Fe-B magnet. However, it is composed on expensive and rare-earth metals. On the other hand, low-temperature phase (LTP) MnBi is a promising rare-earth free permanent magnet. Another advantage of LTP MnBi is as temperature raises, both its coercivity and energy product increase, which makes it an ideal material for engine application. Therefore, here we choose LTP MnBi as the core hard magnet. On the other hand, we use FeCo and Co as the shell soft magnets because of their high magnetization [22]. In order to make exchange coupling structure, here we proposed two techniques, swaging and jump sputtering.

1. SWAGING

Swaging is a mechanical deformation process, which is good for elongate and condense particle samples. The processes of mixing and swaging particles are described in figure 2-2. Properties of MnBi, FeCo and Co nanoparticles are shown in figures 2-3 and 2-4. The sample geometry and packing degree were shown in figure 2-5. Figure 2-6 shown the properties of swaged MnBi/FeCo nanoparticle mixture and heat treated MnBi/Co swaged nanoparticle mixture. It is shown that the magnetization of swaged sample is higher than particle mixture. It also shown that heat treatments can effectively enhance sample's magnetic properties. The sample annealed at 300 °C shown decreased magnetic properties. This is because LTP MnBi starts to decompose so its composition and crystal structure were degraded.

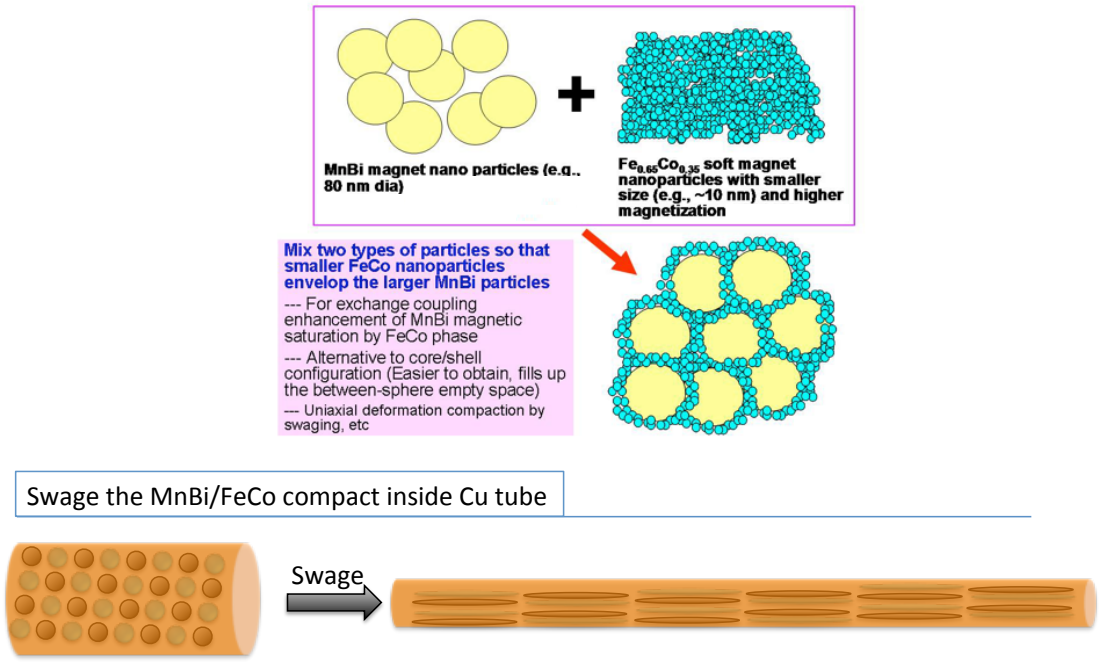

Figure 2-2 The processes of mixing and swaging particles into bulk magnets.

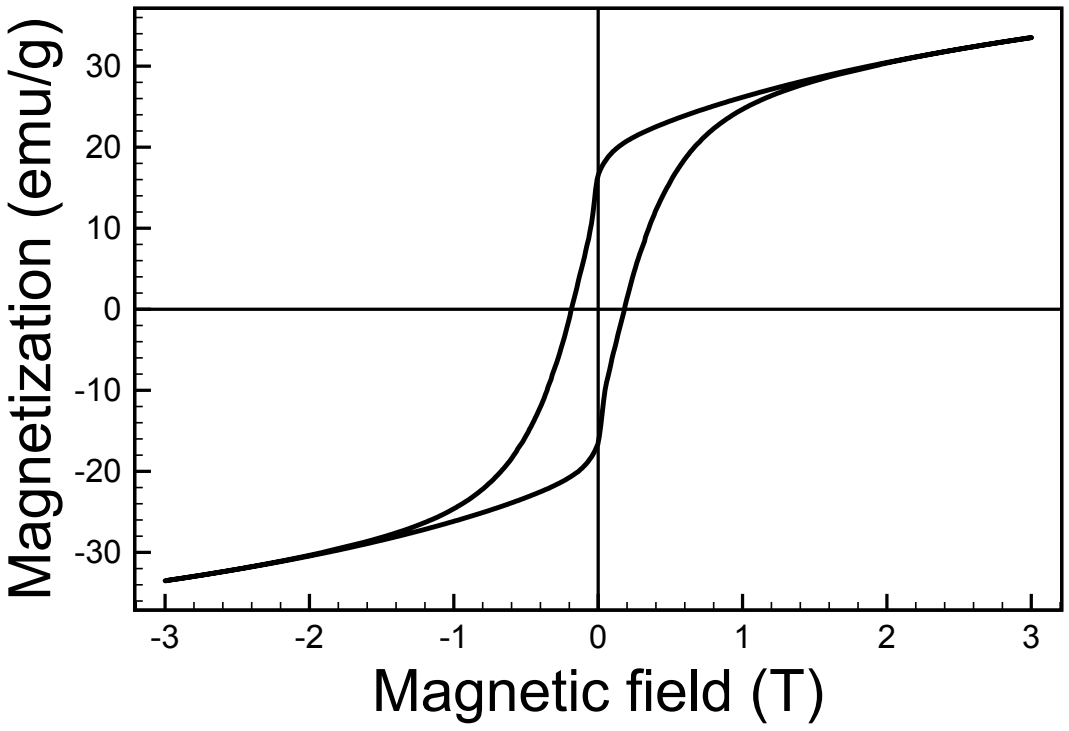

Figure 2-3 Magnetic properties of MnBi nanoparticles.

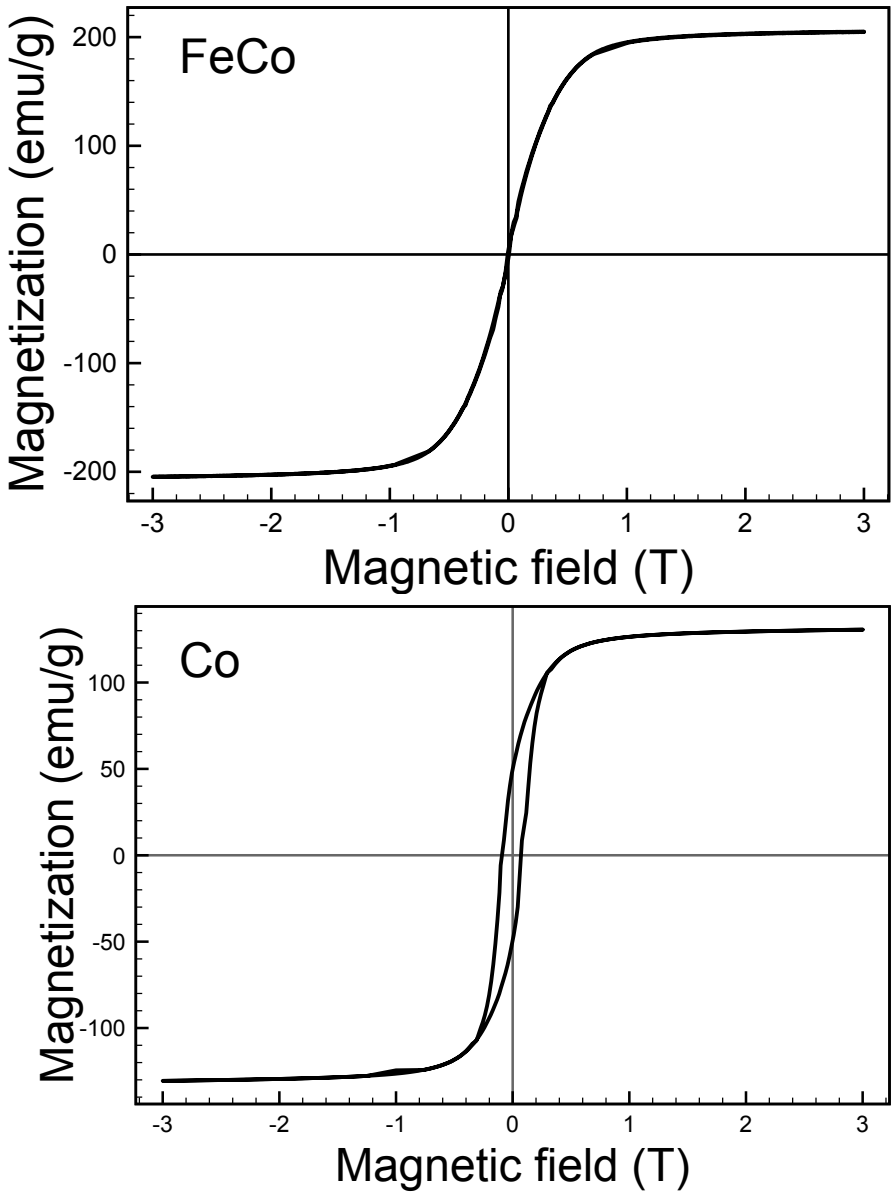

Figure 2-4 Magnetic properties of FeCo and Co nanoparticles.

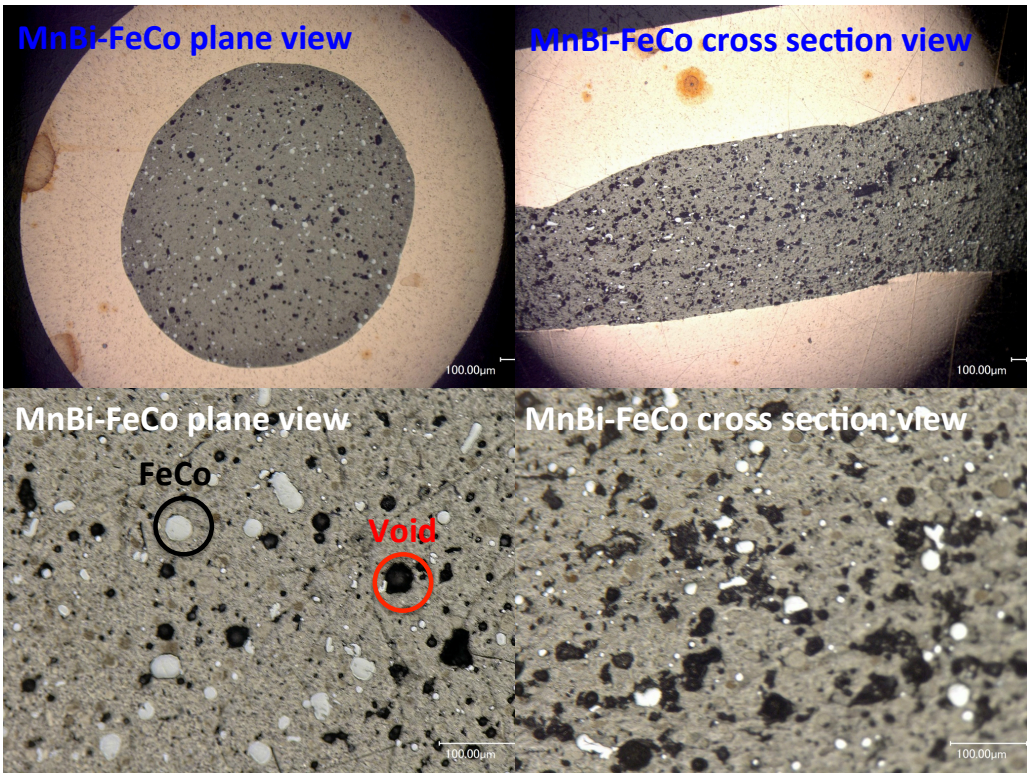

Figure 2-5 Swaged sample geometry and packing degree.

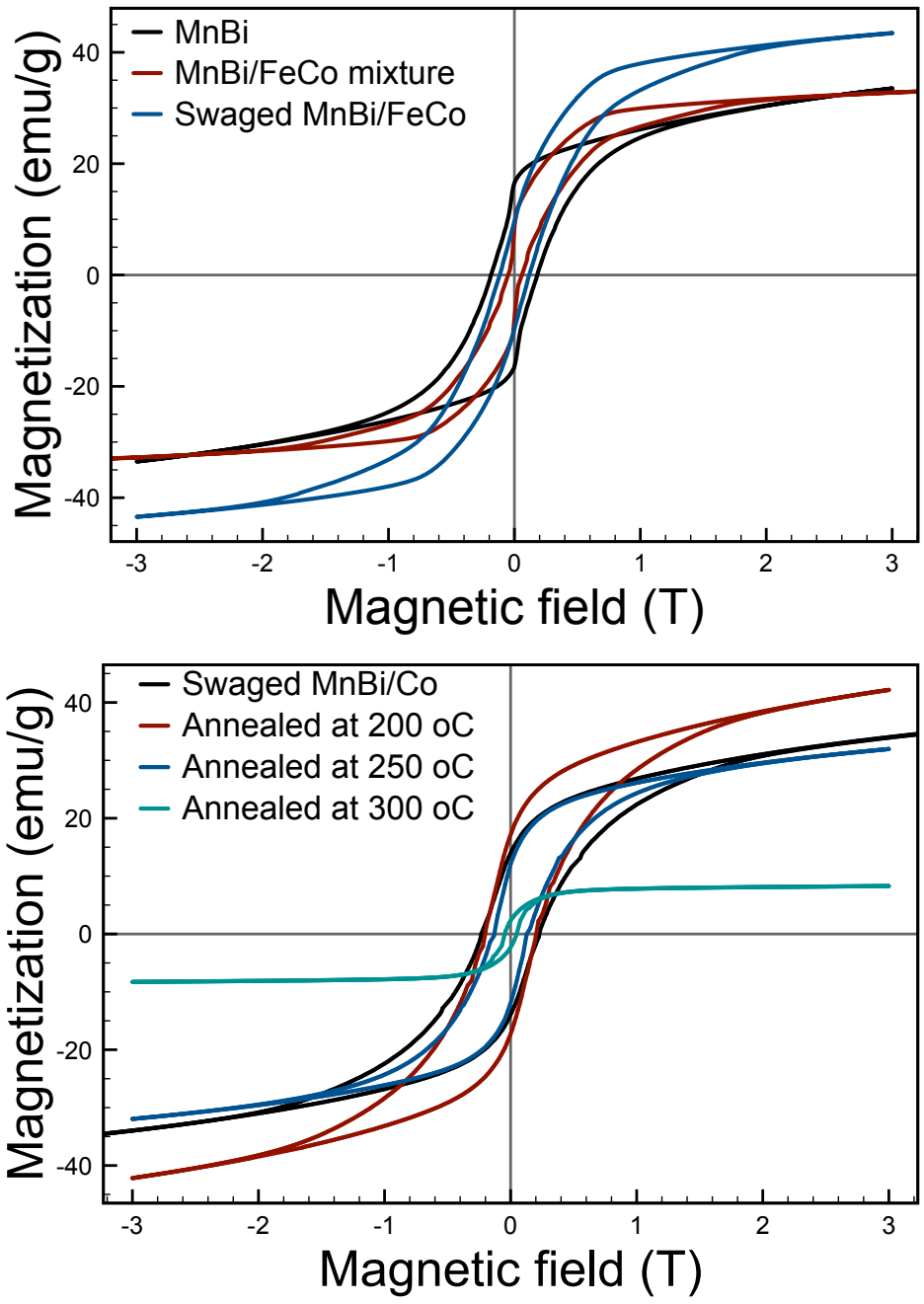

Figure 2-6 Properties of swaged MnBi/FeCo nanoparticle mixture and annealed MnBi/Co swaged nanoparticle mixture.

2. JUMP SPUTTERING

Jump sputtering is a novel sputtering process specially designed for particle samples. As illustrated in figure 2-7, particles are agitated by the vibrator underneath the sputtering chamber. Desired shell material was sputter coated onto those particles while they were jumping and flipping. Figure 2-8 shown magnetic properties and geometry of MnBi starting microparticles. MnBi microparticles were fabricated by attrition milling for 12 to 48 hours and particle size ranges from less than 100 nm to few micrometer. Figure 2-9 (a) shown Transmission Eelectron Microscopy (TEM) image of MnBi particles coated with a thin shell of FeCo. Figure 2-9 (b) and (c) shown the EDS results of FeCo coated MnBi particles. It is obvious that FeCo were uniformly coated on MnBi particles. Figure 2-10 shown the magnetic properties of as milled MnBi particles and MnBi particles coated with FeCo shell. MnBi bulk was milled for 12 hours, which render particle size from 200 nm to few micrometer. The thickness of FeCo shell was determined by TEM to be 2 nm. After jump sputtering, magnetization increased from 20 emu/g to almost 50 emu/g while the coercivity only decreased for few percent. Figure 2-11 shown the magnetic properties of as milled MnBi particles and MnBi particles coated with FeCo shell. MnBi bulk was milled for 48 hours, which render particle size below 100 nm. After jump sputtering, magnetization increased from 6 emu/g to almost 20 emu/g and the coercivity stay the same.

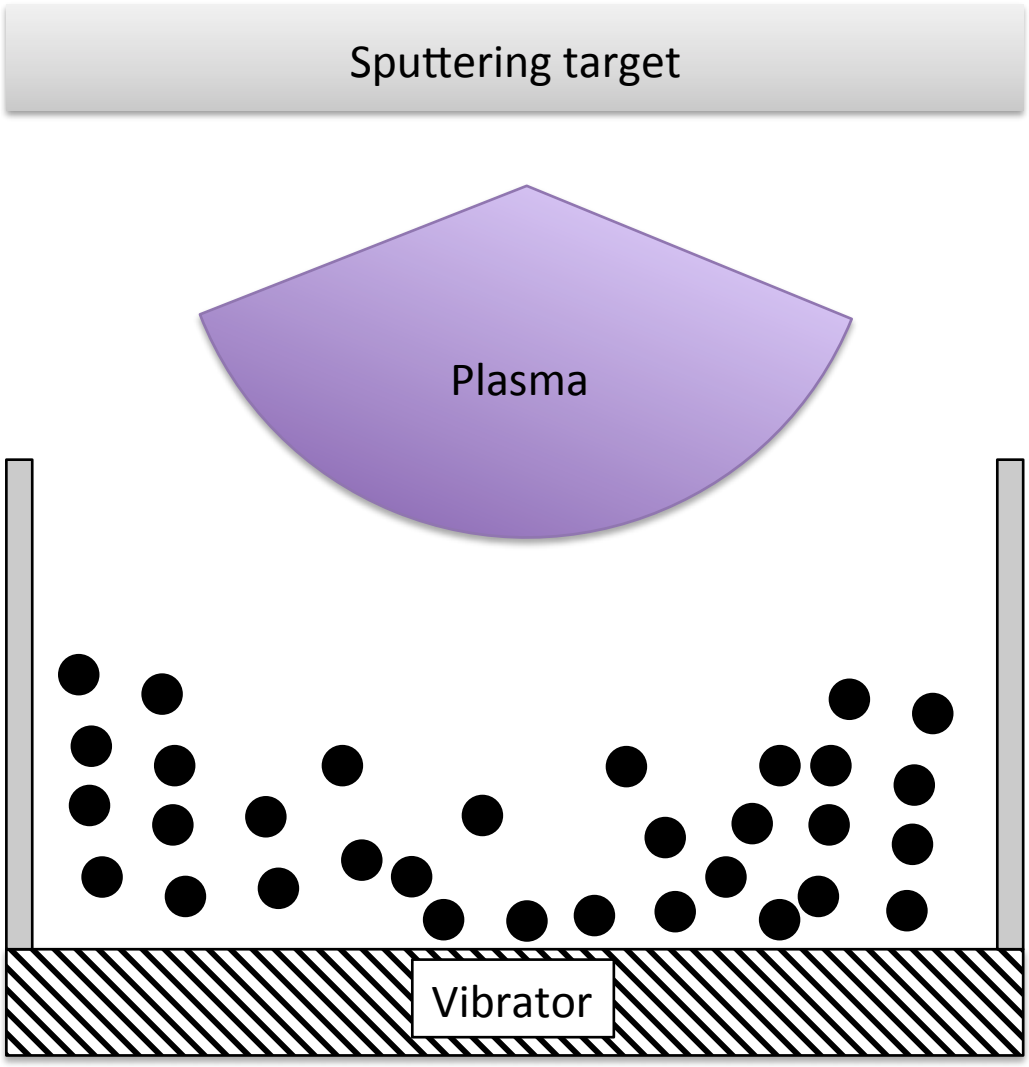

Figure 2-7 Jump sputtering process. Particles were agitated by vibrator underneath the sputtering chamber and then coated with plasma material.

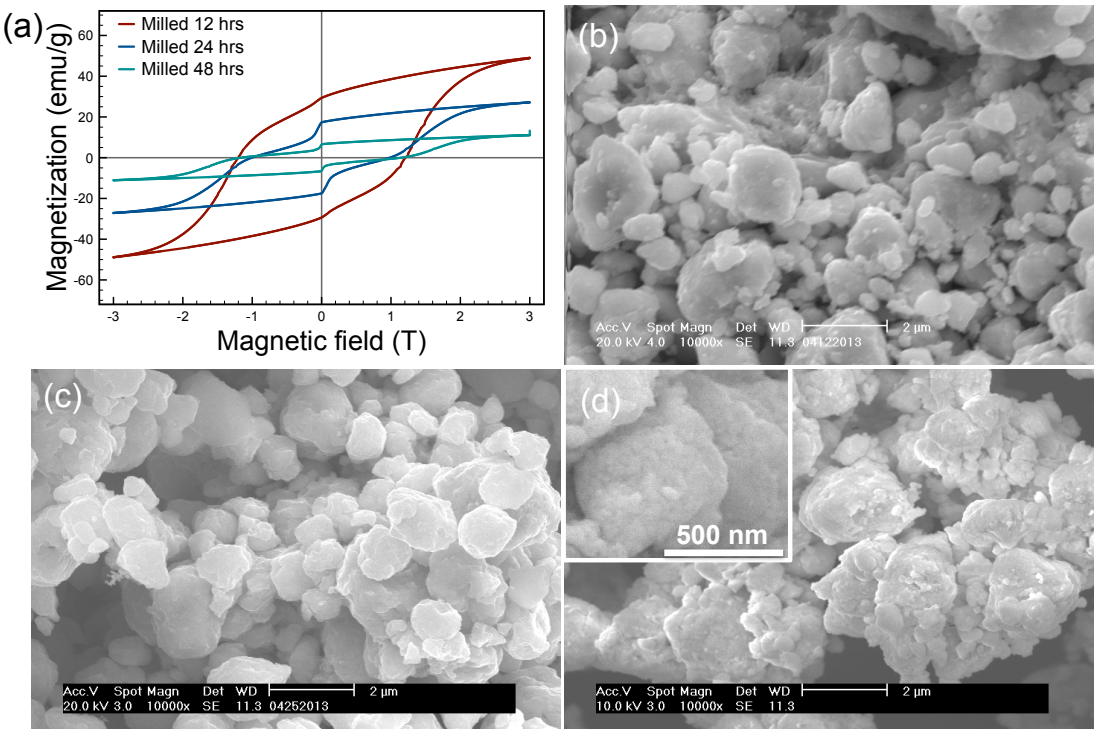

Figure 2-8 Magnet properties and size geometry of attrition milled MnBi particles. (a). Magnetic properties of MnBi particles milled for 12, 24 and 48 hours. (b). Geometry of MnBi particles milled for 12 hours. (c). Geometry of MnBi particles milled for 24 hours. (d). Geometry of MnBi particles milled for 48 hours.

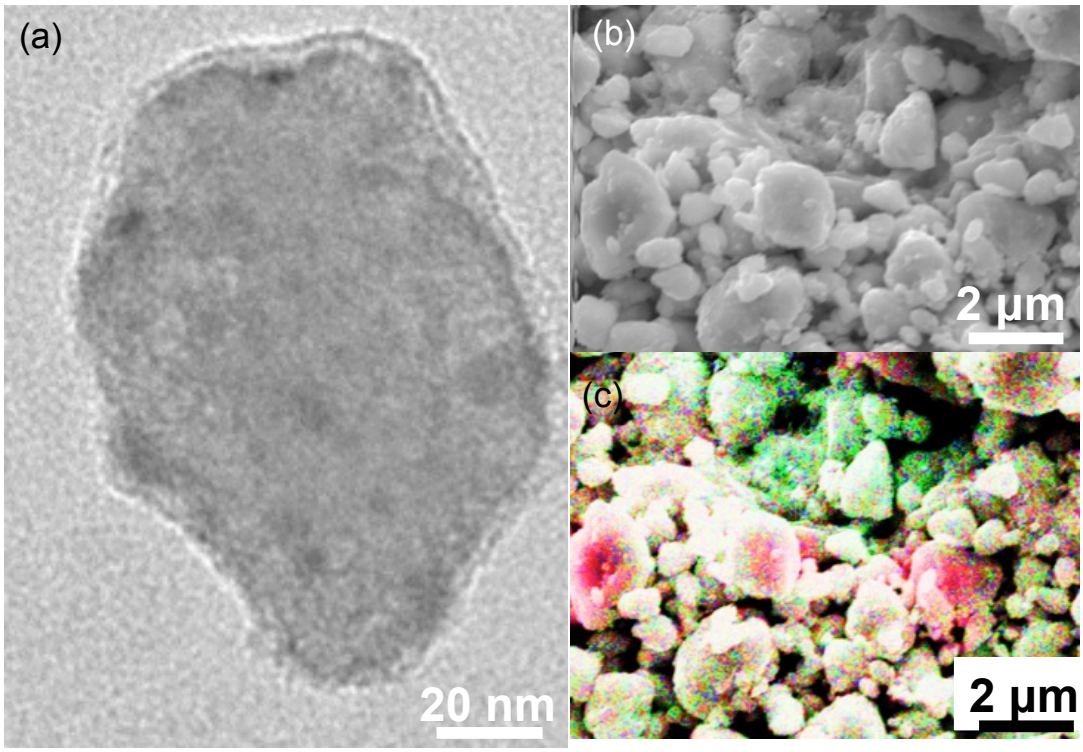

Figure 2-9 Particles geometry and elemental mapping on FeCo coated MnBi particles. (a). TEM image of FeCo coated MnBi particles. The thickness of FeCo coating was found to be less than 2 nm. (b) & (c). Elemental mapping on FeCo coated MnBi particles, which shown distribution of Mn (red), Bi (green), Fe (blue) and Co (black).

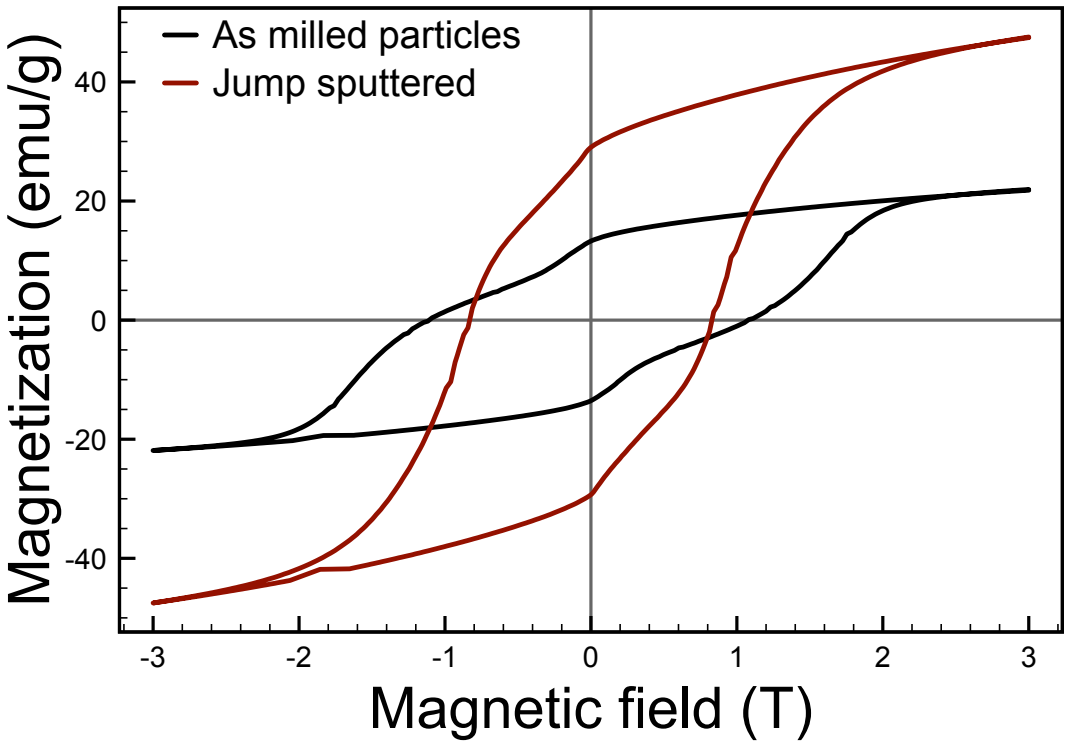

Figure 2-10 shown the magnetic properties of as milled MnBi particles and MnBi particles coated with FeCo shell. MnBi bulk was milled for 12 hours, and thickness of FeCo is 2 nm.

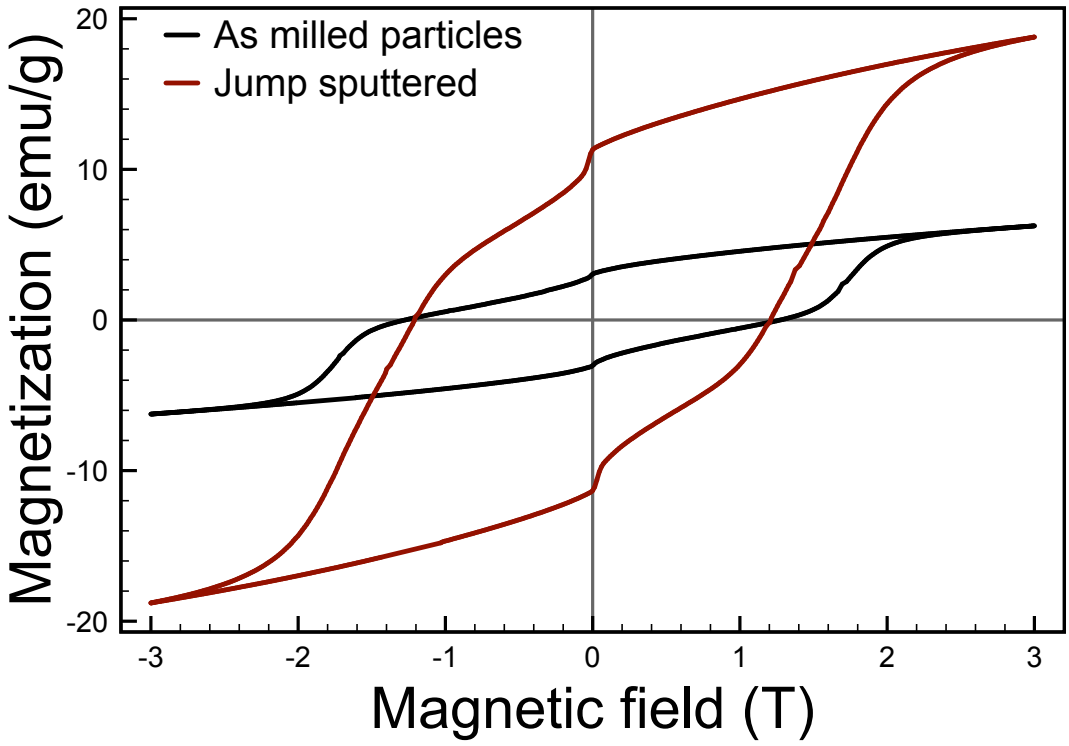

Figure 2-11 Shown the magnetic properties of as milled MnBi particles and MnBi particles coated with FeCo shell. MnBi bulk was milled for 48 hours.

3. SPARK EROSION

For NdFeB, it is interesting to study magnetic properties of its nanoparticles. People proposed several different ways to create NdFeB nanoparticles, such as mechanical milling [23], chemical synthesis [24], and mechanical synthesis [25]. However, milling process cannot render high amount of NdFeB nanoparticles and chemical synthesis has low yield.

In order to produce high quality NdFeB nanoparticles at high production yield, here we applied a novel spark erosion process. Figure 2-12 (a) shown the setup of spark erosion chamber. Both spark erosion electrodes and spark erosion charges were soaked in liquid nitrogen and the electrodes are connected with capacitors and the whole chamber was vibrating during the sparking process. When fully charged spark erosion charges getting closer to each, an electric field was built up in between. Once electric field exceeds the breakdown voltage of the dielectric liquid nitrogen, spark occurs. Because spark is high temperature plasma, it will evaporate the spark erosion materials. Those vaporized materials were quenched by liquid nitrogen then condensed into nanoparticles. Figure 2-12 (b) shown the chamber during spark erosion.

Figure 2-13 shown SEM image of spark eroded Nd-Fe-B nanoparticles. Table 2-1 shown the composition of both Nd-Fe-B bulk and nanoparticles and the ratio before and after spark erosion is similar to each other.

Figure 2-14 shown the HRTEM images and diffraction pattern of Nd-Fe-B nanoparticles. The particles size is between 10 nm to 50 nm and shows $Nd_2Fe_{14}B$ crystal structure.

Figure 2-15 shown size distribution of Nd-Fe-B spark eroded particles. The percentage of nanometer size particles is almost 25 percent to the total production yield. We can easily separate these nanoparticles from microparticles by sieving with appropriate mesh sets.

Figure 2-16 shown M-H loops of Nd-Fe-B nanoparticles produced at different spark erosion conditions. All particles have similar magnetization M_s. Figure 2-17 shown how coercivity and spark erosion power are related. As spark erosion power increases, the coercivity decreases. Figure 2-18 (a) – (d) shown the X-ray diffraction pattern, M – H loop and particle geometry of Nd-Fe-B spark eroded particles before and after annealing. As indicated in figure 2-18 (a), the crystal structure didn't changed after heat treatment. As shown in figure 2-18 (b), magnetization did increased after annealing. By comparing particle geometries from figures 2-18 (c) and (d), it is clear that particles were agglomerated after annealing. Figure 2-19 shown the trend of coercivity after annealing and it is obvious that coercivity of annealed particles increases as the annealing temperature. We can control magnetization and coercivity of nanoparticles by adjusting process conditions and post annealing conditions.

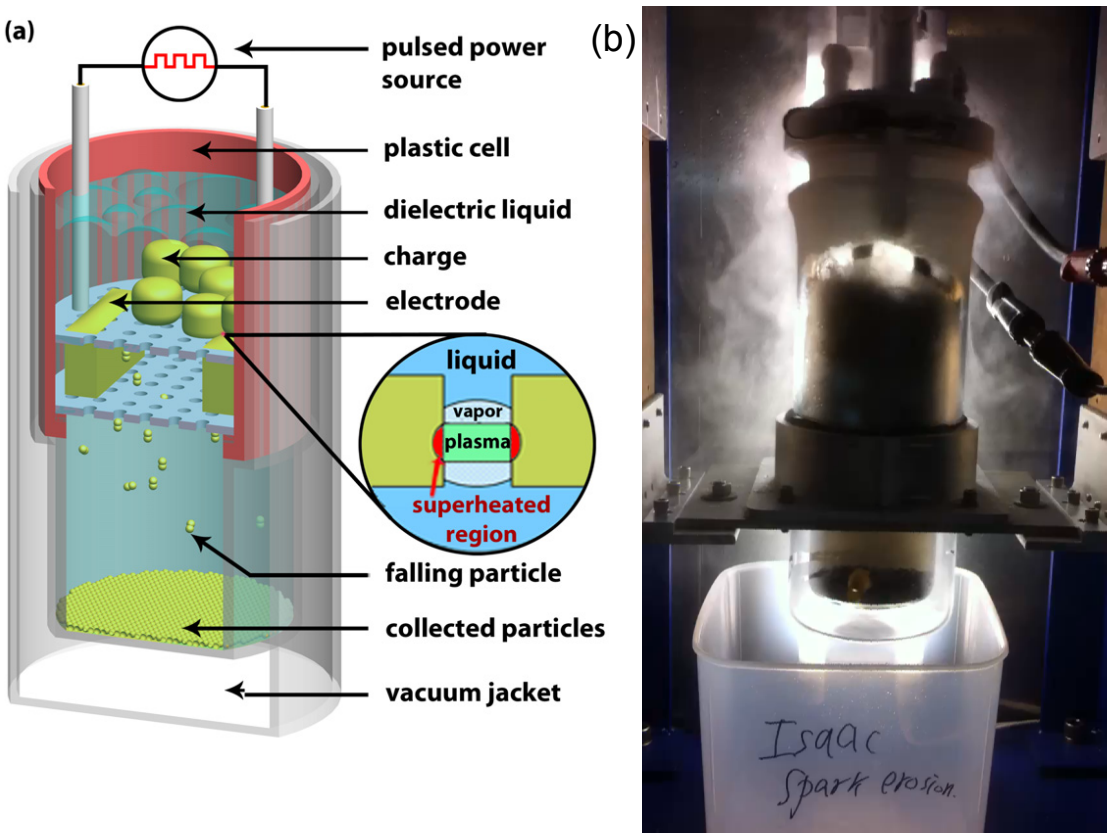

Figure 2-12 Spark erosion process setup. (a). Layer by layer description of spark erosion chamber. (b). Spark erosion chamber during sparking process.

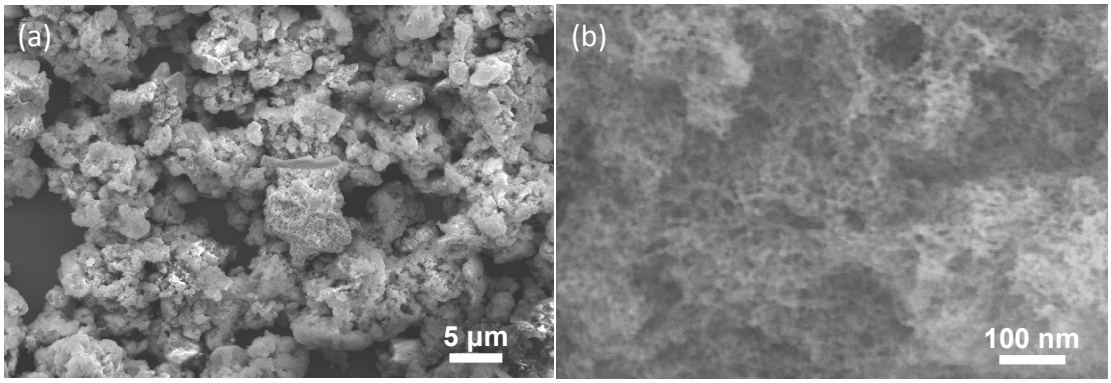

Figure 2-13 Spark eroded Nd-Fe-B particles geometry. (a). low magnification. (b). High magnification.

Table 2-1 Nd-Fe-B bulk and spark eroded particle composition.

Nd-Fe-B samples composition

	Nd	Fe	B	Al	Cu
K&J Nd-Fe-B magnet	**1.67**	**13.16**	**1.13**	**0.36**	**0.04**
Spark erosion particles	**1.70**	**12.99**	**1.49**	**0.33**	**0.06**
Melting point (^{o}C)	**1,021**	**1,538**	**2,076**	**660**	**1,085**

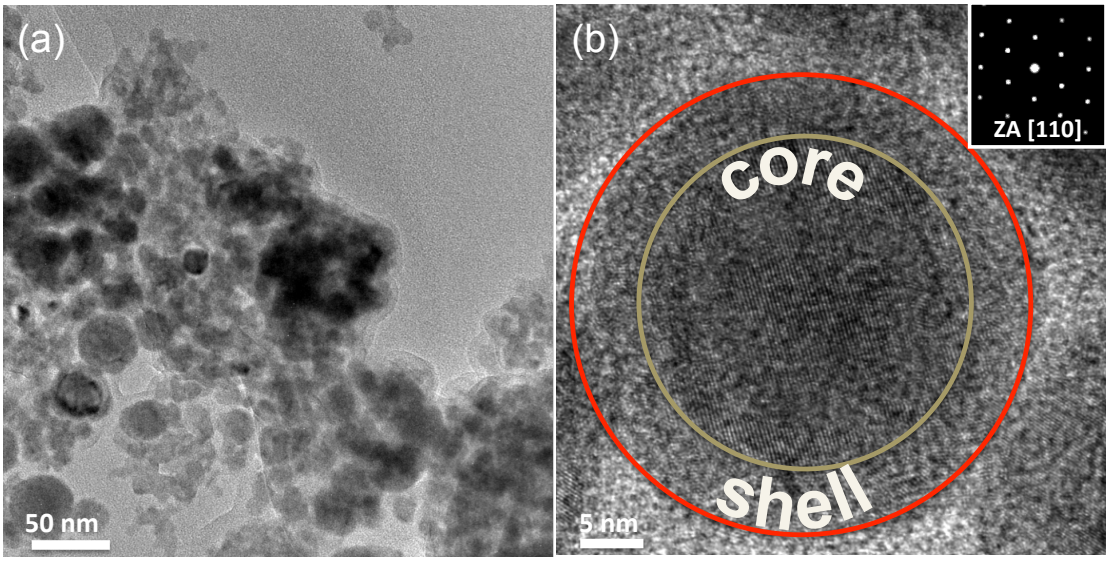

Figure 2-14 High resolution TEM images of spark eroded Nd-Fe-B nanoparticles. (a). Nanoparticles size distribution. (b). Atomic arrangement of spark eroded Nd-Fe-B nanoparticles with zone axis at [110].

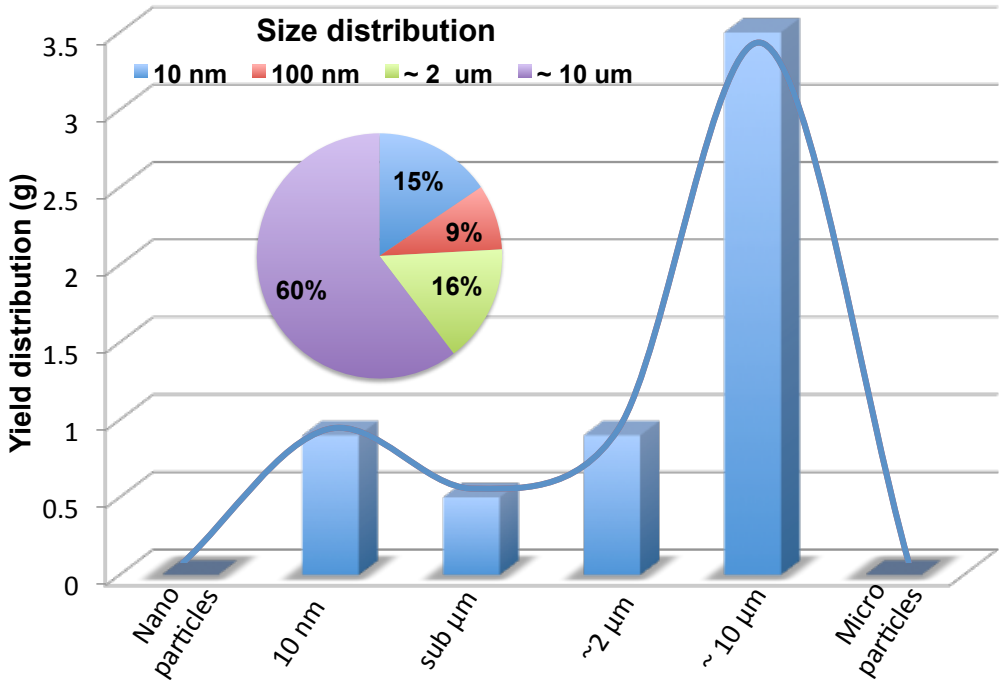

Figure 2-15 Size distribution of Nd-Fe-B spark eroded particles.

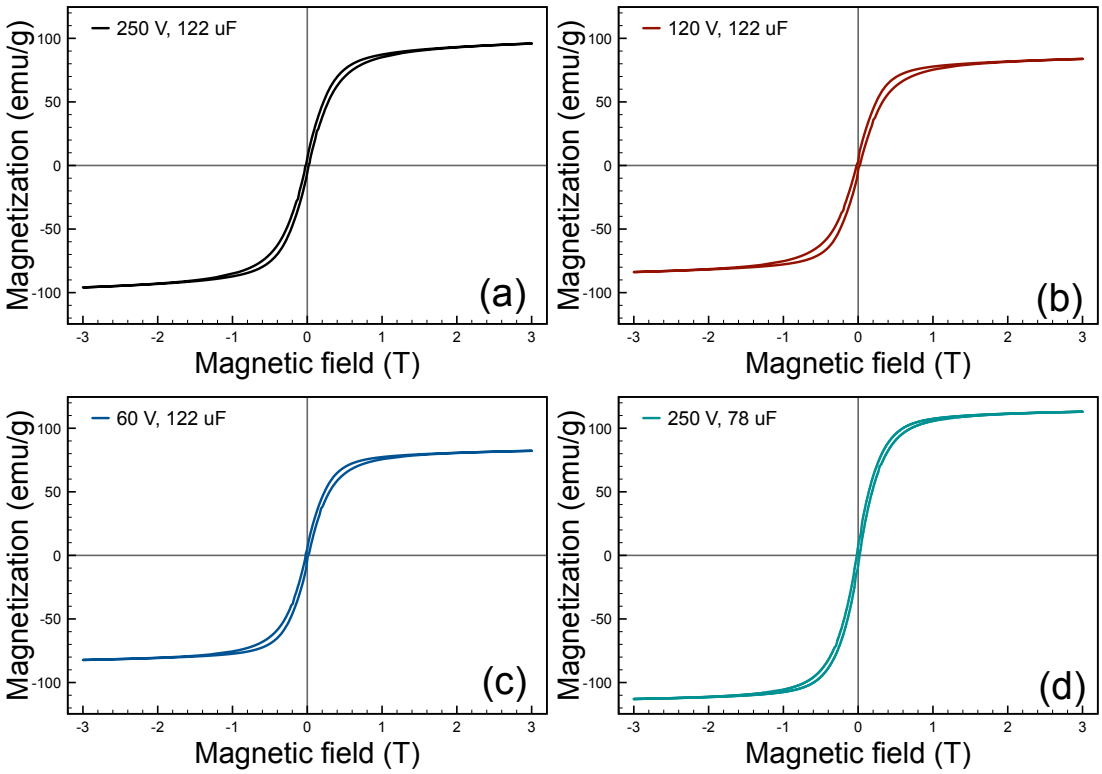

Figure 2-16 Magnetic properties of Nd-Fe-B particles fabricated under different spark erosion conditions.

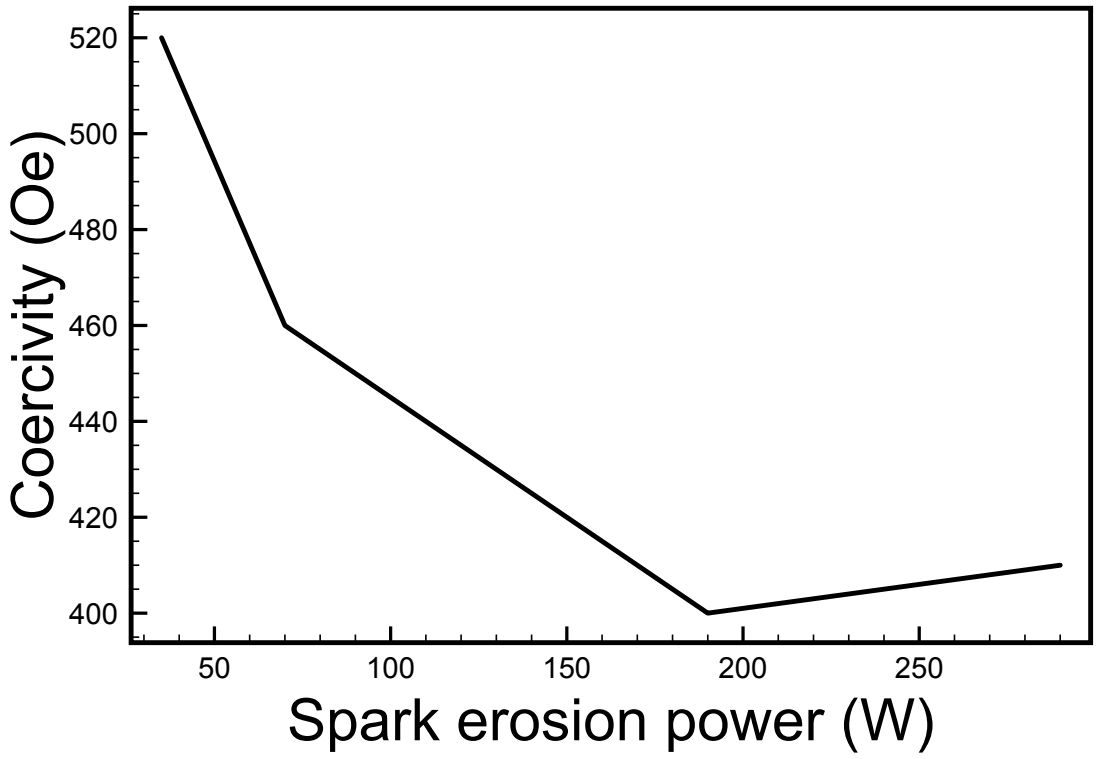

Figure 2-17 Relationship between Nd-Fe-B spark erosion particle's coercivity and spark erosion power.

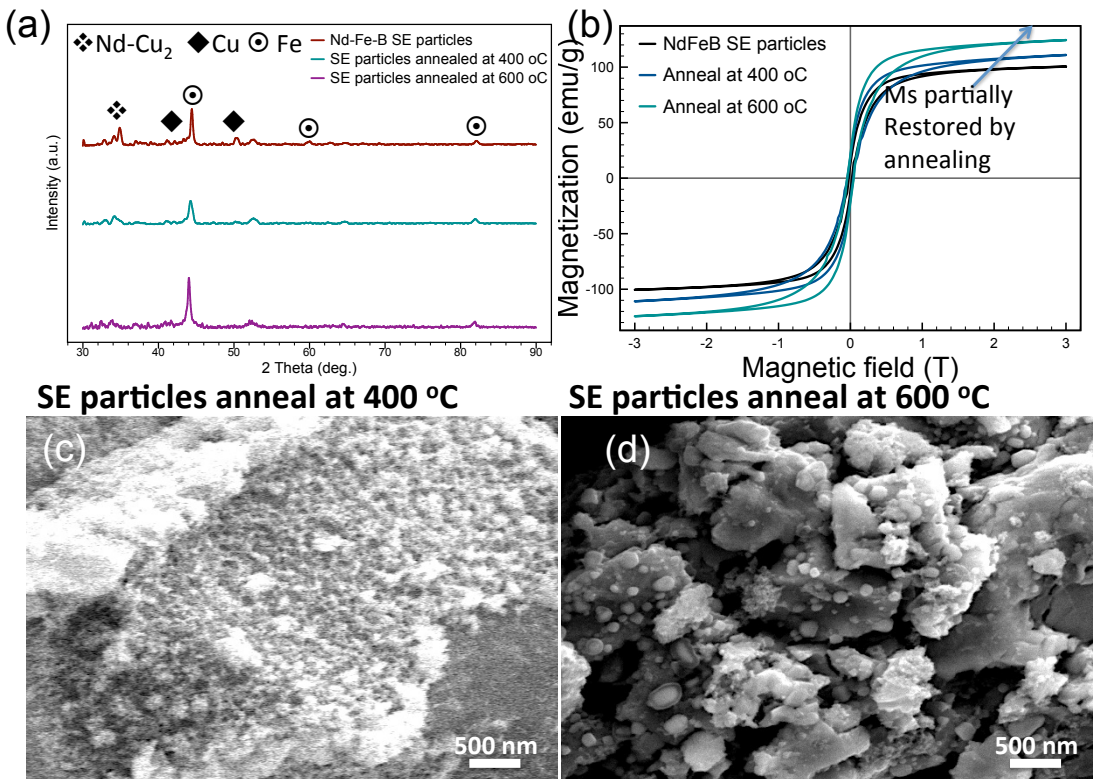

Figure 2-18 Nd-Fe-B spark eroded particles properties vs annealing temperature. (a). Crystal structure of as sparked and post annealed Nd-Fe-B particles. (b). Magnetic properties of as sparked and post annealed Nd-Fe-B particles. (c). Nd-Fe-B particles annealed at 400 °C. (d). Nd-Fe-B particles annealed at 600 °C.

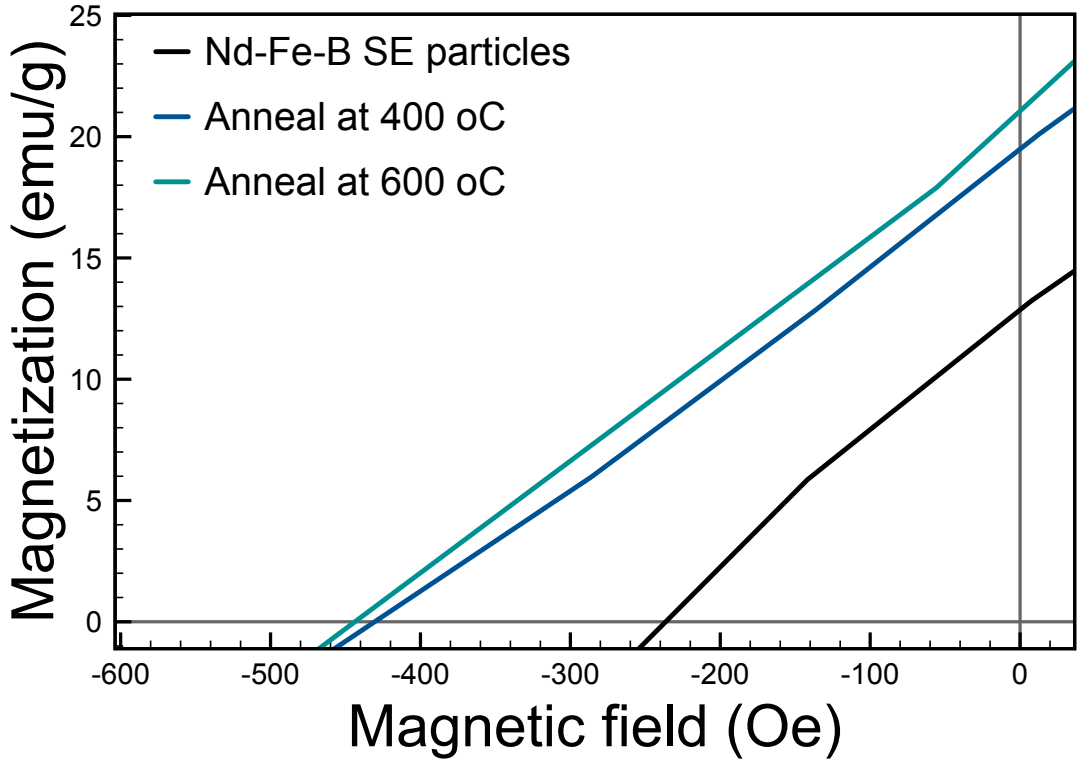

Figure 2-19 Magnetic properties of Nd-Fe-B spark eroded particles before and after annealing.

ACKNOWLEDGEMENTS

This research was funded by Depart of Energy (DOE) under APAR-E project and IWAMA fund from UCSD.

Chapter 2, in part, is currently being prepared for submission for publication of the material. The dissertation author was the primary investigator and author of this paper. Co-author include Sungho Jin.

CHAPTER 3: THERMOELECTRIC PROPERTIES OF SPARK ERODED N-TYPE HALF-HEUSLER NANOPARTICLES

INTRODUCTION

Thermoelectric materials have been extensively studied as a promising candidate for renewable energy applications [1]. It has the potential to convert waste heat into usable energy so as to enhance overall energy efficiency. Public transportation and high temperature industry processes are two major sources of global energy consumption and large amount of waste heat was produced by these two sectors [2]. For example, the surface temperature of locomotive vehicle wheels can be as high as 750 °C [3], air and gas exiting from jet engine can easily be heated up close to 600 °C [4], and recovery of waste heat from industrial activities involved in blast furnace and casting processes at temperatures higher than 600 °C was reported[5, 6]. In order to convert these high temperature waste heat into energy, it is necessary to study thermoelectric materials that has high performance at 500 °C to 800 °C.

Widely studied thermoelectric materials can be categorized by their working temperature, for example, Bi-Sb-Te ternary alloy: near room temperature to 200 °C [7], Pb-Te binary alloy: from ~300 °C to ~500 °C [8], Skutterudite alloy: from 400 °C to 600 °C [9], half-Heusler alloy: from 500 °C to 800 °C [10, 11], and Si-Ge compound > 800 °C [12]. MNiSn (M= Hf, Zr, Ti) is an n-type half-Heusler alloy with reported ZT = 1 at 500 °C to 800 °C [10, 11, 13]. It is possible to tailor its performance by doping [14], grain boundary engineering [15], or controlling its

effective mass and enhance phonon scattering at point defects and grain boundaries [10]. Here we propose a robust way to produce half-Heusler nanoparticles and apply coil-heating assisted hot press to make bulk samples with nanostructure and study the effects of microstructure, carrier concentration and hot press conditions on thermoelectric properties.

METHODOLOGY

1. MATERIALS

The starting material was prepared by ACI Alloys, INC. Hf, Zr, Ni, Sn, Sb with purity 99.9% were weighted according to the composition of $Hf_{8.2}Zr_{24.6}Ni_{32-2}Sn_{34.5}Sb_{0.5}$ and then the mixture of all components was arc melted at least three times to enhance homogeneity. The molten alloy was then quenched and solidified into rectangular ingots and button shape ingots.

2. SPARK EROSION

Spark erosion is a robust way of producing nanoparticles and details were described in previous reports [7, 16]. In this research, we used $Hf_{8.2}Zr_{24.6}Ni_{32-2}Sn_{34.5}Sb_{0.5}$ half-Heusler (HH) as both spark erosion electrodes and spark erosion charges. Spark erosion materials, both the rectangular electrodes and button-shaped charge materials, were then placed in a quartz pot container filled with liquid nitrogen dielectric medium. The spark erosion electrodes were connected to charged capacitors for controlled sparking. Because liquid nitrogen is boiling so it can push away air and oxygen to make the spark erosion environment a nitrogen gas environment. Also, the low temperature of liquid nitrogen, -196 °C, prevents spark erosion materials from being oxidized during spark erosion

process. The quartz pot was custom designed with a vacuum jacket to minimize boiling and enhance preservation of liquid nitrogen. A custom made mechanical shaker was then attached onto the quartz pot to produce collisions among neighboring HH alloy button ingots and electrodes. Sparks were produced when electric field across charged HH ingots exceed the breakdown field of liquid nitrogen. These sparks are actually high temperature plasma (with the estimated temperature on the order of 10,000 °C), which can melt and vaporize spark erosion electrodes and charges. These molten and vaporized spark erosion materials were immediately quenched by liquid nitrogen and condensed into nanoparticles. After spark erosion, the quartz pot was hermetically sealed with a customized glass cap to boil off residual liquid nitrogen through bubbler. The sealed spark erosion pot was then transferred into glove box, which has oxygen level lower than 0.5 ppm.

3. PARTICLE SIZE SELECTION

Particles were then collected and sieved inside glove box. Particles were first sieved with a sieve assembly to 625 mesh to remove large particle agglomerations.

4. HOT PRESS

HH nanoparticles were loaded into a graphite die and pressed with a coil-heating assisted hot press into disk pellets inside a glove box. The pressure was held at 80 MPa while the pellet was heated to 550 °C − 1,100 °C. The holding time at peak temperature was 2 minutes and pellets were air cooled to room temperature.

5. CHARACTERIZATION

Current, voltage and power of each spark were recorded by oscilloscope (Tektronix TDS2012B). Spark erosion nanoparticles size and microstructure of hot pressed samples were evaluated with scanning electron microscopy (SEM, FEI XL30). Crystal structures of half-Heusler samples were characterized by Bruker D2 Phaser X-ray diffractometer (XRD) with Cu K_α (λ=0.154 nm) as the radiation source and θ-2θ scan range was set from 20° to 80°. Sample density was measured by Archimedes' method. Thermal diffusivity (D) was measured along the press direction by laser flash (LFA457, Netzch). Both electrical conductivity (σ) and Seebeck coefficient (S) were measured by ZEM-3 (ZEM-3, ULVAC). Specific heat (C_p) was measured by DSC-404 (DSC-404, Netzch). The measurement uncertainties of electrical conductivity, thermal diffusivity and specific heat estimated to be 3% and 5% for Seebeck coefficient and the resulting uncertainty of ZT is 11%. All thermoelectric properties were measured from room temperature to 700 °C.

Figure 3-1 (a) shown the setup of spark erosion and a spark was also recorded in this figure. With transparent quartz pot, we can observe how sparks were produced at different voltage, capacitance and shaking frequency. We can also monitor the dielectric medium level through this transparent quartz pot to ensure consistency of spark erosion process. Vacuum jacket can enhance thermal insulation of the quartz pot so that it can effectively preserve liquid nitrogen dielectric medium. Figure 3-1 (b) shown the discharging current, discharging voltage and spark power of a typical spark and we can control these

properties by adjusting our customized power supply. The discharging current, discharging voltage and power of this recorded spark were 2.5 A, 300 V, 920 W, respectively. Figures 3-2 (a) and (b) shown the size and geometry of uniformly dispersed spark eroded HH nanoparticles. The particles size was found to be smaller than 20 nm.

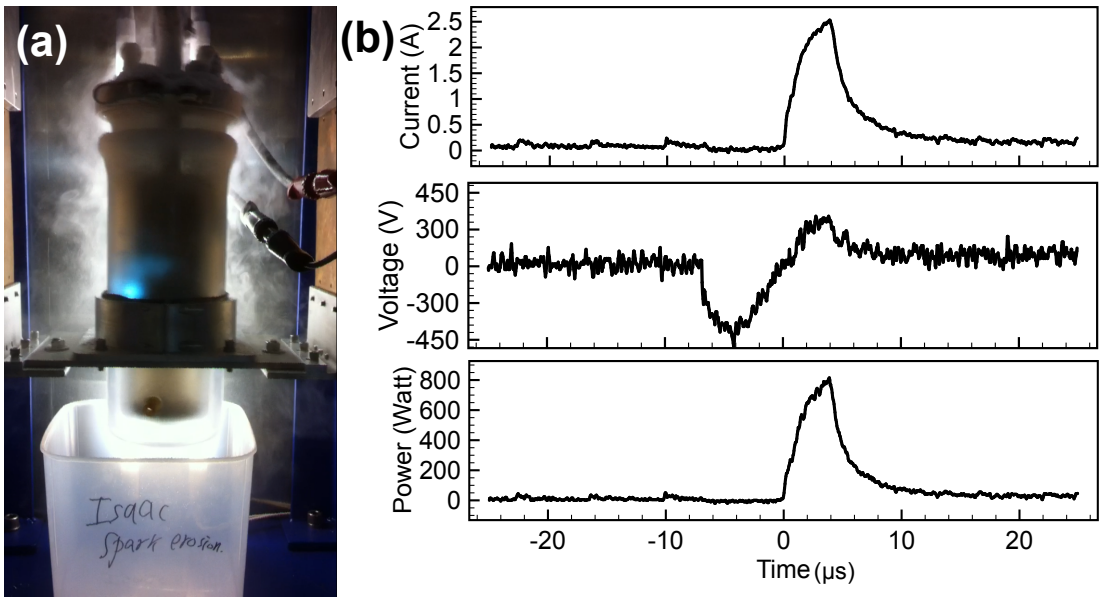

Figure 3-1 Spark erosion process setup and current, voltage and power of sparks. (a) The spark erosion setup. Both spark erosion electrodes and charges were placed inside the quartz pot which is filled with liquid nitrogen dielectric medium. Transparent quartz pot allows direct see-through observation of the spark erosion process, (b) For this typical spark, its discharging current, voltage and power are 2.5 A, 300 V and 920 Watt, respectively.

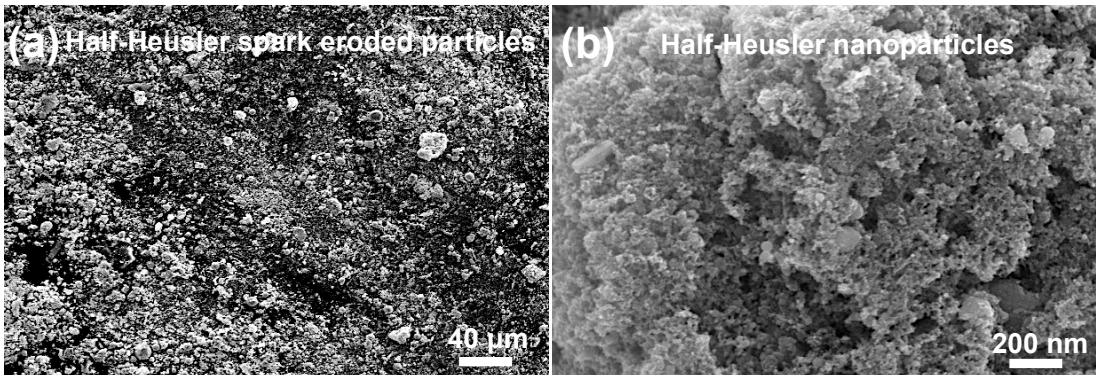

Figure 3-2 Half-Heusler spark erosion particle size analysis. (a) Particle size uniformity confirmed by low magnificent image, (b) The average particle size is smaller than 20 nm.

HH nanoparticles were hot pressed at elevated temperature, 550 °C (HH550) and 1,100 °C (HH1100) into disk pellets. Density of HH550 and HH1100 were measured to be 6.600 (g/cm^3) and 8.435 (g/cm^3), respectively. Figures 3-3 (a) and (b) show microstructures of HH550 and HH1100, respectively. These two figures indicate that HH550 has lower density, smaller grain and relative porous microstructure as compared to HH1100. Figure 3-3 (c) is X-ray diffraction patterns of as-received HH bulk material, spark eroded HH nanoparticles and hot pressed HH pellets. HH nanoparticles and hot pressed pellets were composed mainly of half-Heusler Ni-Sn-Zr phase and both Hf_6-Ni-Sb_2 and Ni_3Sn_4 phases were also found in these pellets. These Sn and Sb rich phases can enhance carrier concentration in HH nanoparticles and hot pressed pellets [10]. Figure 3-3(d) shown the thermal conductivity of HH550 and HH1100 samples. Thermal conductivity of both samples was first decrease with rising temperature due to shorter relaxation time of phonons at high temperature and then increase with rising temperature because of bipolar thermal conductivity. HH550 has lower thermal conductivity than HH1100 because its grain size is smaller and density is lower.

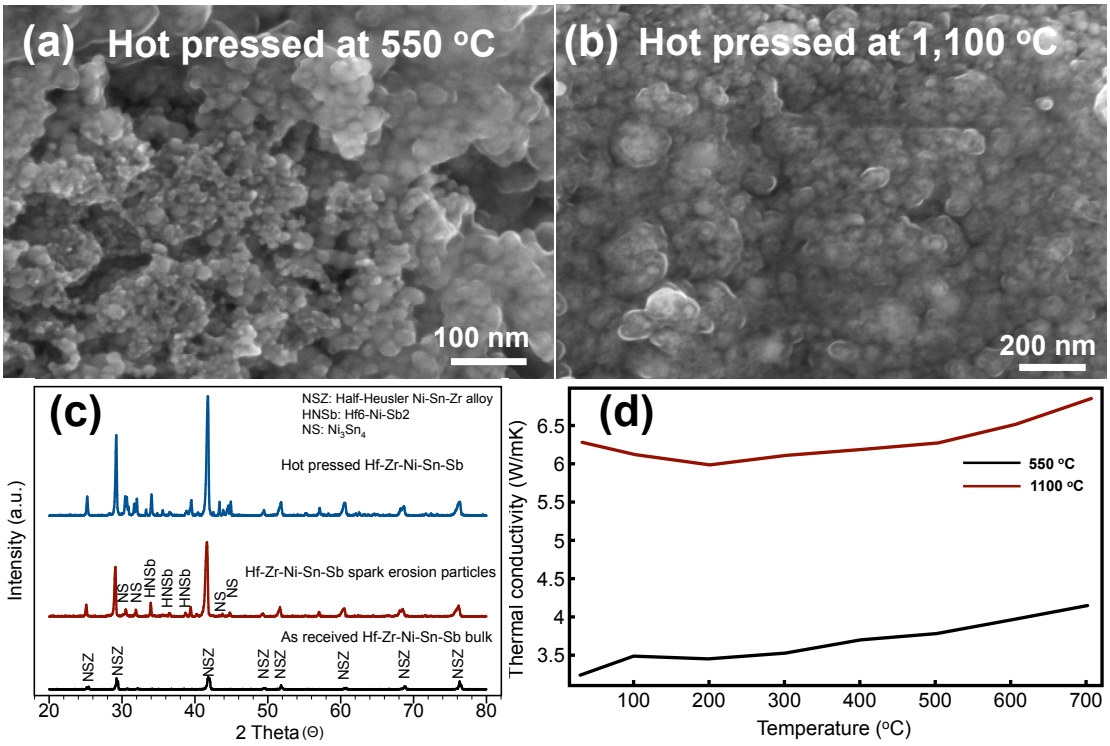

Figure 3-3 Microstructure, x-ray diffraction pattern and thermal conductivity of half-Heusler nanoparticles. (a) Microsturcure of half-Heusler nanoparticles hot pressed at 550 °C , (b) Microstructure of half-Heusler nanoparticles hot pressed at 1,100 °C, (c) X-ray diffraction pattern of half-Heusler bulk, nanoparticles and hot pressed disk, (d) Thermal conductivity of hot pressed half-Heusler nanoparticles measured from room temperature to 700 °C.

Figure 3-4 (a) shows Seebeck coefficient of hot pressed samples. For HH550, the Seebeck coefficient increases with temperature up to 400 °C and then decreases as temperature further increased. For HH1100, its Seebeck coefficient increases until 600 °C and then decreases as temperature further increased. The trend transition is related to bipolar transportation, where both contributions of thermally excited electrons and holes became significant and cancelled out each other so that Seebeck coefficient was reduced. Figure 3-4 (b) shows electrical conductivity of HH 550 and HH1100 samples. As the temperature increases, the electrical conductivity decreases because of stronger electron scattering. Once samples were heated to above 300 °C, the slope of σ/T became less negative, which is due to a gradually increased carrier concentration from thermal excitation. Carrier concentration was further increased when samples were heated to higher than 600 °C. Power factor of both samples were recorded in figure 3-4 (c). The highest power factor of HH550 and HH1100 in this paper was 10 and 34 (10^{-4} W/mK^2), respectively. As indicated in Figure 3-4 (c), the onset temperature of bipolar effect for HH550 and HH1100 was 300 °C and 600 °C, respectively. We can calculate the thermoelectric figure of merit (ZT) value with above mentioned Seebeck coefficient, electrical conductivity and thermal conductivity, and the results are plotted in Figure 3-4 (d). By optimizing hot press condition, we can enhance ZT from 0.13 to 0.34.

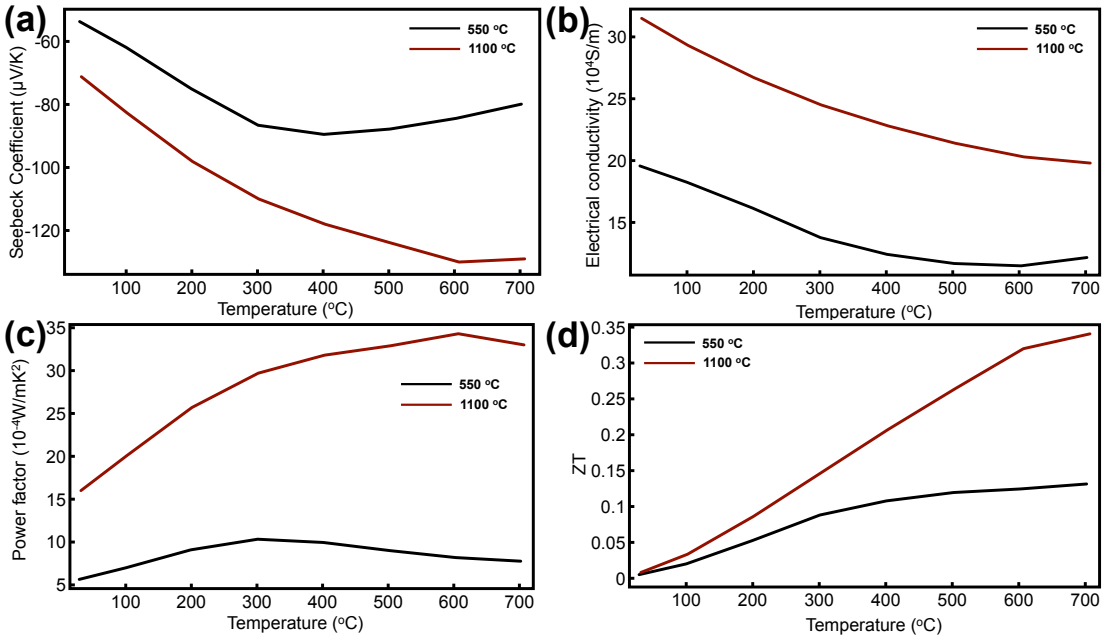

Figure 3-4 Thermoelectric properties of half-Heusler nanoparticles hot pressed at 550 °C and 1,100 °C. (a). Seebeck coefficient, (b). Electrical conductivity, (c). Power factor, (d). ZT value.

The Seebeck coefficient of hot pressed $Hf_{8.2}Zr_{24.6}Ni_{32-2}Sn_{34.5}Sb_{0.5}$ nanoparticles that we have shown here are slightly lower than previous reported data on hot pressed $Hf_{8.6}Zr_{25.9}Ni_{34.4}Sn_{34.1}Sb_{0.3}$ nanoparticles [10]. Because we have more Sb n-type dopant in our alloy, carrier concentration in our alloy is higher and this leads to lower Seebeck coefficient. High carrier concentration in our hot pressed samples also results in higher electrical conductivity than previous reported data [10, 11]. Thermal conductivity of HH550 is 4.2 (W/mK) at 700 ^{o}C, which is the lowest value among half-Heusler alloys ever reported. For HH1100, because grain size was increased after hot press process, so grain boundary scattering was reduced and the thermal conductivity increased. In order to further improve HH nanoparticles' Seebeck coefficient, electrical conductivity and decrease thermal conductivity, we can optimize hot press peak temperature and its holding time at peak temperature to make nanocrystalline samples. It is also possible to further increase ZT by fine tuning of half-Heusler alloy composition to optimize its carrier concentration [10] and by adding high melting point oxides such as ZrO_2 and Al_2O_3 into HH hot press pellets to increase boundary scattering [17]. All related research efforts are currently in progress.

We developed an efficient spark erosion process of making half-Heusler $Hf_{8.2}Zr_{24.6}Ni_{32-2}Sn_{34.5}Sb_{0.5}$ nanoparticles. These nanoparticles were pressed and sintered into disk pellets by coil heating assisted hot press system. Seebeck coefficient, electrical conductivity and thermal conductivity were measured from room temperature to 700 ^{o}C and the highest figure of merit ZT achieved in this research is 0.34 at 600 ^{o}C. It is possible to further increase pellets' thermoelectric

properties by optimizing hot press holding time, hot press peak temperature and half-Heusler alloy composition.

ACKNOWLEDGMENTS

The authors acknowledge the financial support of this work by General Engineering & Research, L.L.C., under a grant from the Department of the Navy, Naval Research Laboratory, and Iwama Endowed Fund at UC San Diego.

Chapter 3, in full, is currently being prepared for submission for publication of the material. The dissertation author was the primary investigator and author of this paper. Co-authors include DongWon Chun, Renkun Chen and Sungho Jin.

.

CHAPTER 4: CONCLUSIONS

We have designed and developed novel functional materials for different applications. Universal solder can bond onto both metal and inorganic substrates and can potentially re-innovate the packaging industry. Permanent magnet with high energy product $(BH)_{max}$ can decrease energy consumption and overall product weight for various motors and generators. Thermoelectric materials can enhance energy efficiency by transforming wasted heat to renewable energy. With all these improved functional materials, we can fabricate high performance electrical devices, lower energy consumption and enhance energy efficiency.

REFERENCES

[1] Abtew M, Selvaduray G. Lead-free solders in microelectronics. Materials Science & Engineering R-Reports. 2000;27:95-141.

[2] Zeng K, Tu KN. Six cases of reliability study of Pb-free solder joints in electronic packaging technology. Materials Science & Engineering R-Reports. 2002;38:55-105.

[3] Laurila T, Vuorinen V, Kivilahti JK. Interfacial reactions between lead-free solders and common base materials. Materials Science & Engineering R-Reports. 2005;49:1-60.

[4] John L. Vossen WK. Thin Film Processes II: Academic Press, INC.; 1991.

[5] Tang W, He A, Liu Q, Ivey DG. Room temperature interfacial reactions in electrodeposited Au/Sn couples. Acta Materialia. 2008;56:5818-27.

[6] Mavoori H, Ramirez AG, Jin S. Universal solders for direct and powerful bonding on semiconductors, diamond, and optical materials. Applied Physics Letters. 2001;78:2976-8.

[7] Mavoori H, Ramirez AG, Jin SH. Lead-free universal solders for optical and electronic devices. Journal of Electronic Materials. 2002;31:1160-5.

[8] Ramirez AG, Mavoori H, Jin SH. Bonding nature of rare-earth-containing lead-free solders. Applied Physics Letters. 2002;80:398-400.

[9] Mahmudi R, Geranmayeh AR, Salehi M, Pirayesh H. Impression creep of the rare-earth doped Sn-2%Bi lead-free solder alloy. Journal of Materials Science-Materials in Electronics. 2010;21:262-9.

10] Yoshio Waseda MI. Purification Process and Characterization of Ultra High Purity Metals: Application of Basic Science to Metallurgical Processing. Germany: Springer; 2002.

[11] Zhao N, Huang ML, Zhong Y, Ma HT, Pan XM. Effects of rare earth Ce addition on the microstructure, wettability and interfacial reactions of eutectic Sn–0.7Cu solder. J Materials Science-Materials in Electronics. 2015;26:345-52.

[12] Li G, Li Z, Li H, Shi Y. Development of an Er-doped Mg–Zn–Al solder by ultrasonic treatment and its joint property. Materials Letters. 2014;136:59-62.

[13] Li Y, Wong CP. Recent advances of conductive adhesives as a lead-free alternative in electronic packaging: Materials, processing, reliability and applications. Materials Science and Engineering: R: Reports. 2006;51:1-35.

[14] Villars P. ASM Handbook Volume 03: Alloy Phase Diagrams1992.

[15] Thomas RB. Free energy of formation of binary compounds : an atlas of charts for high-temperature chemical calculations. Cambridge, MASS.: MIT Press; 1971.

[16] Matsuura Y. Recent development of Nd–Fe–B sintered magnets and their applications. Journal of Magnetism and Magnetic Materials. 2006;303:344-7.

[17] Kramer MJ, McCallum RW, Anderson IA, Constantinides S. Prospects for Non-Rare Earth Permanent Magnets for Traction Motors and Generators. JOM. 2012;64:752-63.

[18] Sagawa M, Hirosawa S, Yamamoto H, Fujimura S, Matsuura Y. Nd-Fe-B Permanent Magnet Materials. Japanese Journal of Applied Physics. 1987;26:785.

[19] Tian Z, Li S, Peng K, Gu B, Zhang J, Lu M, et al. The microstructure and magnetic properties of NdFeB magnets directly solidified at a low cooling rate. Materials Science and Engineering: A. 2004;380:143-6.

[20] Hono K, Sepehri-Amin H. Strategy for high-coercivity Nd–Fe–B magnets. Scripta Materialia. 2012;67:530-5.

[21] Kneller EF, Hawig R. The exchange-spring magnet: a new material principle for permanent magnets. Magnetics, IEEE Transactions on. 1991;27:3588-60.

[22] Zeng H, Li J, Liu JP, Wang ZL, Sun S. Exchange-coupled nanocomposite magnets by nanoparticle self-assembly. Nature. 2002;420:395-8.

[23] Nilay GA, George CH, David JS. Novel Nd2Fe14B nanoflakes and nanoparticles for the development of high energy nanocomposite magnets. Nanotechnology. 2010;21:295705.

[24] Deheri PK, Swaminathan V, Bhame SD, Liu Z, Ramanujan RV. Sol−Gel Based Chemical Synthesis of $Nd_2Fe_{14}B$ Hard Magnetic Nanoparticles. Chemistry of Materials. 2010;22:6509-17.

[25] Pal A, Gabay A, Hadjipanayis GC. Mechanochemical synthesis of Nd2Fe14B alloy with high coercivity. Journal of Alloys and Compounds. 2012;543:31-3.

[26] Bell LE. Cooling, Heating, Generating Power, and Recovering Waste Heat with Thermoelectric Systems. Science. 2008;321:1457-61.

[27] Laboratory LLN. U. S. Energy Flow. 2013.

[28] Cole KD, Tarawneh CM, Fuentes AA, Wilson BM, Navarro L. Thermal models of railroad wheels and bearings. International Journal of Heat and Mass Transfer. 2010;53:1636-45.

[29] Pasini S, Ghezzi U, Andriani R, Ferri LDA. Heat recovery from aircraft engines. Energy Conversion Engineering Conference and Exhibit, 2000 (IECEC) 35th Intersociety. 2000;1:546-53 vol.1.

[30] Barati M, Esfahani S, Utigard TA. Energy recovery from high temperature slags. Energy. 2011;36:5440-9.

[31] Norgate TE, Xie D, Jahanshahi S. Technical and economic evaluation of slag dry granulation. AISTech - Iron and Steel Technology Conference Proceedings. 2012:35-46.

[32] Nguyen PK, Lee KH, Moon J, Kim SI, Ahn KA, Chen LH, et al. Spark erosion: a high production rate method for producing Bi0.5Sb1-5Te3 nanoparticles with enhanced thermoelectric performance. Nanotechnology. 2012;23.

[33] Pei Y, LaLonde AD, Heinz NA, Snyder GJ. High Thermoelectric Figure of Merit in PbTe Alloys Demonstrated in PbTe–CdTe. Advanced Energy Materials. 2012;2:670-5.

[34] Tan G, Liu W, Wang S, Yan Y, Li H, Tang X, et al. Rapid preparation of CeFe4Sb12 skutterudite by melt spinning: rich nanostructures and high thermoelectric performance. Journal of Materials Chemistry A. 2013;1:12657-68.

[35] Chen S, Lukas KC, Liu W, Opeil CP, Chen G, Ren Z. Effect of Hf Concentration on Thermoelectric Properties of Nanostructured N-Type Half-Heusler Materials HfxZr1–xNiSn0.99Sb0.01. Advanced Energy Materials. 2013;3:1210-4.

[36] Chen S, Ren Z. Recent progress of half-Heusler for moderate temperature thermoelectric applications. Materials Today. 2013;16:387-95.

[37] Bathula S, Jayasimhadri M, Singh N, Srivastava AK, Pulikkotil J, Dhar A, et al. Enhanced thermoelectric figure-of-merit in spark plasma sintered nanostructured n-type SiGe alloys. journal article. 2012;101:213902.

[38] Uher C, Yang J, Hu S, Morelli DT, Meisner GP. Transport properties of pure and doped MNiSn (M =Zr, Hf). Physical Review B. 1999;59:8615-21.

[39] Muta H, Kanemitsu T, Kurosaki K, Yamanaka S. High-temperature thermoelectric properties of Nb-doped MNiSn (M = Ti, Zr) half-Heusler compound. Journal of Alloys and Compounds. 2009;469:50-5.

[40] Geng H, Meng X, Zhang H, Zhang J. Lattice thermal conductivity of nanograined half-Heusler solid solutions. journal article. 2014;104:202104.

[41] Nguyen P-K, Jin S, Berkowitz AE. MnBi particles with high energy density made by spark erosion. Journal of Applied Physics. 2014;115:17A756.

[42] He Z, Stiewe C, Platzek D, Karpinski G, Müller E, Li S, et al. Effect of ceramic dispersion on thermoelectric properties of nano-ZrO2/CoSb3 composites. Journal of Applied Physics. 2007;101:043707.